Utrecht University

Master Thesis

OPTICAL ANALYSIS OF ION DYNAMICS IN A BATTERY

Author:

Nelfyenny (5045568)

Supervisor 1:

Dr. ir. Sanli Faez

Supervisor 2:

Dr. Peter Ngene

A thesis submitted in fulfillment of the requirements
for the degree of a Master of Science

in the

Experimental Physics

Departement of Physics

Utrecht University

13 February, 2023

Abstract

RFBs have emerged as a promising electrochemical energy storage technology capable of storing renewable energy sources with long charge-discharge cycle life. As a result, battery monitoring systems have become highly significant, particularly in battery research, to evaluate the performance of battery components or materials after many cycles of operation. In this study, we explore the dynamics of the ions within the electrode when the cell is linked to a potential since this parameter can provide information on the electrochemical performance, indicating the reversibility of the ions during operation. The dielectric characteristics of ions, which react to electric potentials, are utilized to track ion movement within the cell using optical microscopy. This property is connected to the polarizability of active particle valence/conduction electrons in electrodes. The cell will be tested using three different electrolytes; NaCl, $FeCl_2$ and $FeCl_3$. The laser beam is shone at electrochemically operating battery particles as they store or release ions, and the scattered light is analysed. According to the experimental results, half-cells with three different electrolyte solutions may flow ions from one electrode to another with currents ranging from 6 μA to 0.5 mA. The modulation signal at 1 Hz is applied to the cell, and the FFT technique is utilized to determine if the ion response can be monitored optically. However, the response of ions to potential changes is unnoticeable visually. Because the scatter signal from the ions is too faint to be caught by the camera, the amplitude noise from the light source becomes more dominating.

Acknowledgement

In this part, I would like to express my gratitude to the Indonesia Endowment Fund for Education (LPDP), which has agreed to fund me so that I can finish the master's degree at Utrecht University.

Then, I would like to thank to Sanli Faez and Peter Ngene, as my supervisors for guiding me in the experimental process until the completion of this thesis.

I also would like to thank to Nanophotonics group, especially for the EPICs team; Zhu, Anna, Baqis, Hendrik, Ingmar and Danny for their assistance with laboratory work and thesis writing. Also to Aaron, Dante and Paul who have helped a lot in the installation process of measurement setups and understanding of electronics and Python programming.

My gratitude also goes to William Hayes, without whom I would have struggled to comprehend chemical issues, as well as his capacity to overcome problems that arose throughout the experimental procedure. Thank you for always being a great partner and motivating me to keep on track with my thesis project.

Indonesian friends in Utrecht have become a new family, making living abroad in this country simpler and more comfortable. Thank you Sidiq and Nada for constantly providing feedback on thesis writing, Ikhwan for always being a discussion partner and study buddy, and Felicia for making the last few months of thesis completion more enjoyable.

Finally, I want to thank my family, especially my parents and my siblings who never stop praying for me, my husband, and my two daughters who have waited patiently for me for the past two years.

Contents

Chapter 1

Introduction

For recent years, there has been an increase in research on Redox Flow Batteries (RFBs)[1] as a promising energy storage system (ESS), in particular for the electrical energy storage needs for renewable energy sources as wind and solar photovoltaic systems. RFB is a rechargeable devices that store chemical energy and convert it into electrical energy through the reversible reduction and oxidation of working electrolytes. RFBs offer a long charge-discharge cycle life and low capital cost which meet the requirement of large-scale grid storage. One of the main characteristics of these batteries is decoupled the energy capacity and power output, which the former are managed by the quantity of redox-active materials kept in external tanks and the latter by the size of current collectors inside RFBs[2].

When RFBs in operation, electrons travel towards the load or voltage source, while positive ions flow from one electrode to the next via the ion exchange membrane, balancing the charge. These ions have optical properties (scattering); they can be detected due to their ability to create contrast with the surrounding environment. Changes in the amount of ions at the electrodes as a result of redox reactions after many cycles, can be used to assess whether the electrolyte or electrode material causes a reduction in cell performance.

Important RFB components that demonstrate electrochemical performance are the mechanical pumps and the electrodes. The pumps are controlled to be balanced with the extrinsic flow rate of the active liquids in the tanks. Whilst the electrodes, where the reduction-oxidation (redox) reaction takes place, have an impact on RFB efficiency (in power and energy) as well as the battery life cycle. A redox-flow battery's electrode features a porous design, which significantly improve RFB performance by providing active surfaces for electrochemical processes and conducting electrons[3,4], which contributes to the charge transfer of the electrochemical cell[5]. In RFBs sytem, the electrodes highlight the performance of RFB, making it worthwhile to study further, particularly, in terms of monitoring technologies, to observe its dynamic change.

In battery research, monitoring techniques are required to determine the performance

of the battery materials used, the electrochemical processes that occur, and the battery's performance when utilized in numerous cycles. Several in-operando imaging techniques were employed in the monitoring system of electrodes. Microscopes widely used to observe the dynamics of ion movement in the Lithium battery under particular circumstances by implementing several techniques such as cryo-transmission electron microscopy which can observe the lithium dendrite growth process in lithium metal electrodes and high-speed synchrotron X-ray diffraction to elucidate the phase transformation/kinetics of electrode materials. However, to characterize the RFB requires a new technique as the one of the electrochemical performance of the RFB depends on the intrinsic charge-transfer kinetic of the active molecules on the electrodes, which are not commonly considered in conventional lithium batteries[1]. A research conducted by Alice et al.[6] introduced an iSCAT (interferometric scattering) microscopy method to observe the dynamic changes that occur in electrodes of Li-ion battery. iSCAT is an imaging approach that uses the elastic scattering of visible light to provide rapid image acquisition, a low-cost imaging platform for observing ion dynamics in electrodes, and high sensitivity. In this study, iSCAT was utilized to resolve nanoscopic lithium-ion dynamics in battery materials using an electrode of Li_xCoO_2 by determining the intensity of the local dielectric properties of the sample material. This research concluded that the electrode showed a significant changes to the electronic and dielectric properties, which allowed optical monitoring during operation. In addition, iSCAT is generally applicable to various types of batteries, making it is a prospective method that can also be employed in RFB.

Herein, this thesis aims to visualize the electrochemical activity within electrode of the all-iron half-cell redox system using iSCAT microscopy during operation. The use of all-iron materials-based electrolytes is an alternative to Vanadium, which has been commercially employed for current RFB. We observe the response of ions by recording a set of images when the battery cell is connected to an electric potential that changes gradually. As part of the measuring procedure, the collected images are subsequently processed using image filtering to remove noise from electronic signals. From this point, we may compute the intensity for each image in a single measurement period and then study how the intensity changes over time in relation to the electric potential changes. According to our hypothesis, the polarisability of ions should cause the intensity of images to fluctuate proportionally to changes in electric potential, demonstrating that the technique used is adequate for tracking the dynamics of ion. This leads to the following research question:

How effective is the iSCAT microscope as an in-situ tool for visualizing electrochemical performance in RFB cells?

The research question will be addressed in this thesis which organized into six chapters, starting with Chapter 1 which provides background research, a study objective, and the research question. Chapter 2 presents a physical explanation of the redox flow battery, as well as an introduction to the all-iron battery and the iSCAT method, which are necessary to comprehend this study. The research method used including characterize the circuit monitoring system consists of the cell made from all-iron electrode and optical microscope system, programming data acquisition and image processing are explained in detail in Chapter 3, followed by Chapter 4 for Optical Characterization and Chapter 5 for Results. At the end, Chapter 6 describes the discussion, research conclusions, and outlook that in light of the experiment results.

Chapter 2

Theory

2.1 Redox Flow Battery (RFB)

RFBs are a promising solution for large-scale and low-cost energy storage, which is required to encourage the use of intermittent renewable sources due to their unique ability to decouple power and energy[7–10]. They are ideal candidates for cost-effective stationary storage, particularly for long discharges and long storage times.

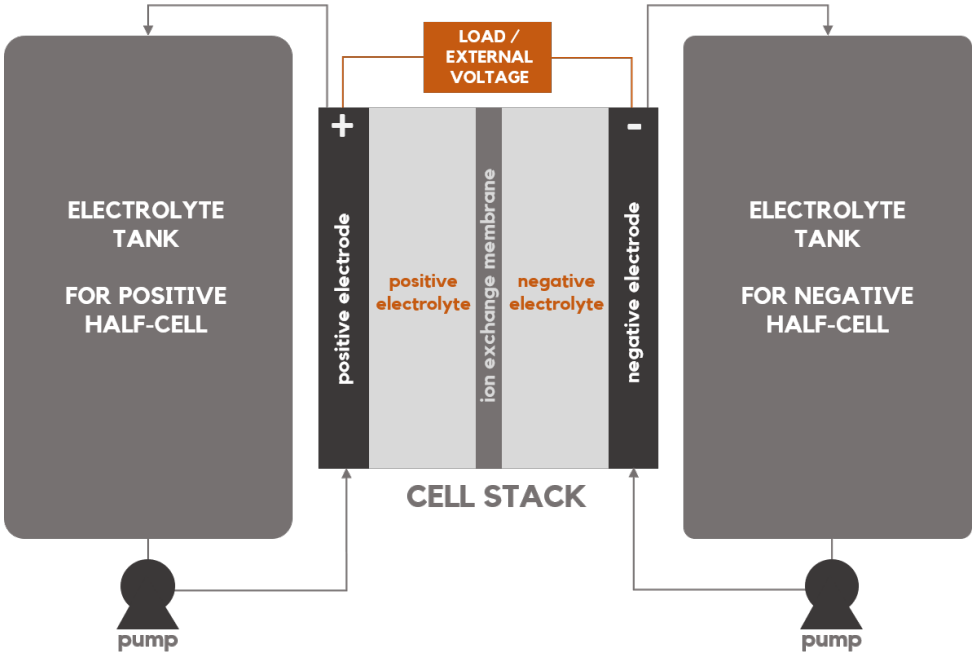

Figure 2.1: Schematic diagram for redox flow battery

An RFB uses two soluble redox couple solutions in each half-cell (see Figure 2.1); all reactants and products are in the solution phase, and no metals are plated on the electrodes. An RFB comprises two mechanical pumps, a membrane or separator called an ion exchange membrane (IEM) and two porous carbon electrodes. The pumps are used to drain the solution and control the balance in its flow rate from the positive tank to the positive cell stack and vice versa during the operation. IEM prevent cross-mixing electrolytes by balancing the exchange membrane of cation and anion. As it limits the

crossing of the active species and offers charge transport channels between the anolyte and catholyte during battery operation, the membrane/separator is an important component of an RFB. High conductivity, high chemical stability, simple process and technology, and low cost are all characteristics of an ideal membrane[11]. Porous electrodes serve as the surface area interface between the electrolyte reactions and the load/external voltage, made from a conductive material. The electrodes, especially those made of carbon[12], significantly improve RFB performance by providing active surfaces for electrochemical processes, distributing liquid electrolytes, cushioning mechanical compression, and conducting electrons and heat[3,4], which contributes to the charge transfer, ohmic and mass transport overpotentials of the electrochemical cell[5]. The

In an RFB, the capacity of the system is governed by the size of the electrolyte tanks, but the system power is dictated by the size of the cell stacks since the redox flow cell stores energy in the solutions[13]. Redox reactions are the chemical reduction and oxidation processes used to store energy in a liquid electrolyte solution that flows through an electrochemical cell battery during charging and discharging. Electrons perform beneficial work by moving via external circuits, while positive ions will diffuse through the membrane separating the two half-cells when the redox reaction is taking place in order to keep the charge neutral and complete the circuit.

During discharging (when a load is connected to the electrodes), electrons flow through the circuit from the negative electrode (anode) to the positive electrode (cathode). While the electrodes are connected, the energy potential in the anode rises, causing electrons to move from the anode to the cathode via oxidation (electrons lost), creating electricity. While the energy potential in the cathode decreases, this results in a reduction (gaining of electrons). During charging (with an external source connected to the electrodes), the reverse reactions occur since the potential in the cathode rises, resulting in the electrons flowing from the cathode to the anode. There will be no more electricity produced after equilibrium is reached in both half-cells because the redox process will stop[14].

One of the most challenging issues for RFB is the cross-contamination of the electrolyte with different elements since the separators are imperfect. Therefore, we will discuss briefly the state-of-the-art of RFB technology namely Vanadium RFB (VRFB). In addition, the RFB made entirely of iron, which will act as the battery's framework in this study, will be discussed.

Vanadium RFB (VRFB)

Currently, the most promising and mature RFB is the all-Vanadium RFB (VRFB). A VRFB single cell is made up primarily of one ion exchange membrane (IEM), two half cells, and two solid electrodes (see Figure 2.2). A VRFB prevents cross-contamination between anolyte (negative electrolyte) and catholyte (positive electrolyte) by using the same two elements for each electrolyte, but with a different oxidation state[9,15]. The anolyte contains Vanadium II-III (bivalent-trivalent, V^{2+} and V^{3+}), while the catholyte contains Vanadium IV-V (tetravalent-pentavalent VO^{2+} and VO_2^+). The electrochemical half-reactions produced in electrodes by these solutions[7]:

$$\begin{aligned} &\text{at cathode:} VO_2^+ + 2H^+ + e^- \overset{\text{discharge}}{\underset{\text{charge}}{\rightleftarrows}} VO^{2+} + H_2O \\ &\text{at anode :} V^{2+} \overset{\text{discharge}}{\underset{\text{charge}}{\rightleftarrows}} V^{3+} + e^- \\ &\text{cathode = positive electrode, anode = negative electrode} \end{aligned} \tag{2.1}$$

Figure 2.2 depicts vanadium ion cycles in a VRFB during operation which corresponds to the reaction in Eq.2.1. In discharging mode, the oxidation occurs in anode resulting loss of electrons from (V^{2+}) to (V^{3+}) and reduction in cathode (gain of electrons, VO_2^+ to VO^{2+}). The Hydrogen ions (H^+) will be diffused from anode to cathode through the IEM, maintaining the charge balance between the negative and positive half cells. In charging mode, the reverse reaction occurs, resulting reduction in anode and oxidation in cathode.

In applications, Vanadium sources are difficult to obtain at a reasonable price, thus for this study, we will use another material with a similar working principle to VFFB but with components that are more abundant and easy to obtain.

Open-source All-iron Battery

In this subsection, we discuss a research conducted by Dipak et al[16] about the improvement of their previous study[17] in open source all-iron battery, as it is our reference in creating our redox flow cell. This research aimed to develop a conventional rechargeable all-iron battery, which suitable for stationary application, that is simple to construct, inexpensive and abundant in materials, and safe to use. The battery cell had a capacity of 80 mAh (degraded to 72 mAh after >1000 cycles) with an open cell potential of 1.1 V. It was

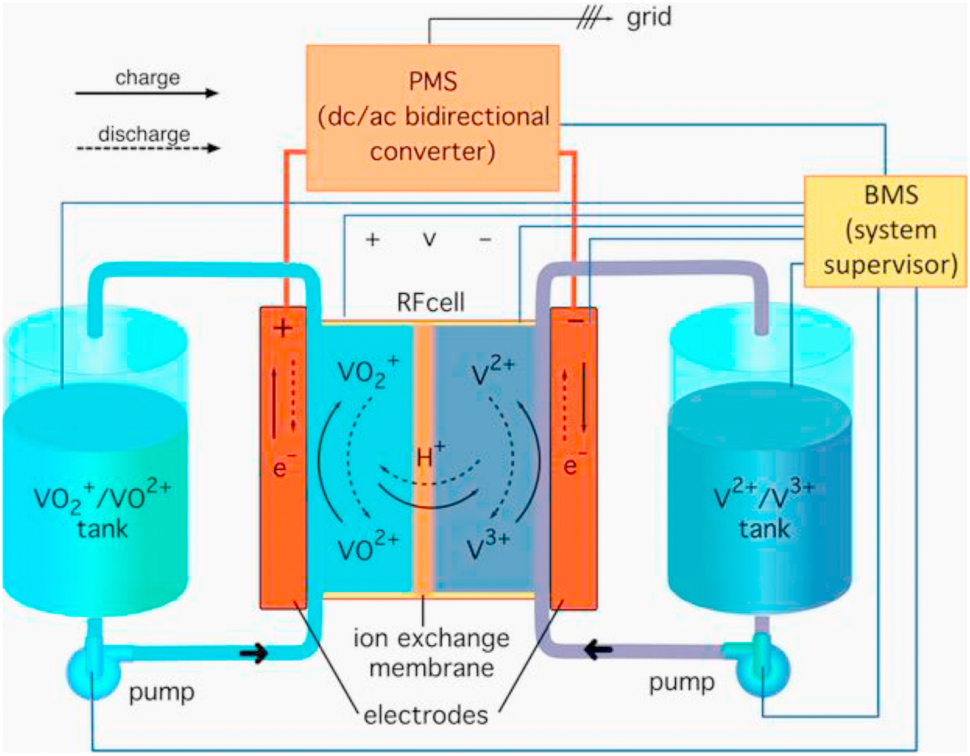

Figure 2.2: The all-vanadium RFB (VRFB) has been the most successful, with commercialization beginning in the 1980s. This scheme depicts a VRFB system with a single-cell electrochemical converter[7]

regarded as relatively stable cell as it only lost 10% of its total capacity.

Figure 2.3a describes the schematic of components for all-iron battery using iron metal (Fe) on anode and ferric iron (Fe^{3+}) on cathode. There were two chemical reagents present: anode electrolyte, the solution in direct contact with the anode (iron metal) electrode made from iron (II) chloride ($FeCl_2$) and cathode electrolyte, made from iron (III) chloride ($FeCl_3$) which in contact with cathode (graphite felt). The high concentration of iron (II) in anode prevented the iron from losing all of its iron permanently and increased reversibility. They also added a ketjen black-conductive carbon (see Figure 2.3b) which allowed electrons to go to the anode and cathode over a much shorter distance. The membrane was subsequently constructed using cellulose acetate drop casting on printing paper, which reduced internal resistance and reduced the voltage drop during discharge.

The operating principle (in terms of redox reaction when the battery connected to load/external voltage) of an all-iron battery is similar to VRFB, however it differs in the presence of a pump. When the battery connected to the load, the iron oxidizes at the anode and reduces an iron salt at the cathode, resulting electron flew from cathode to

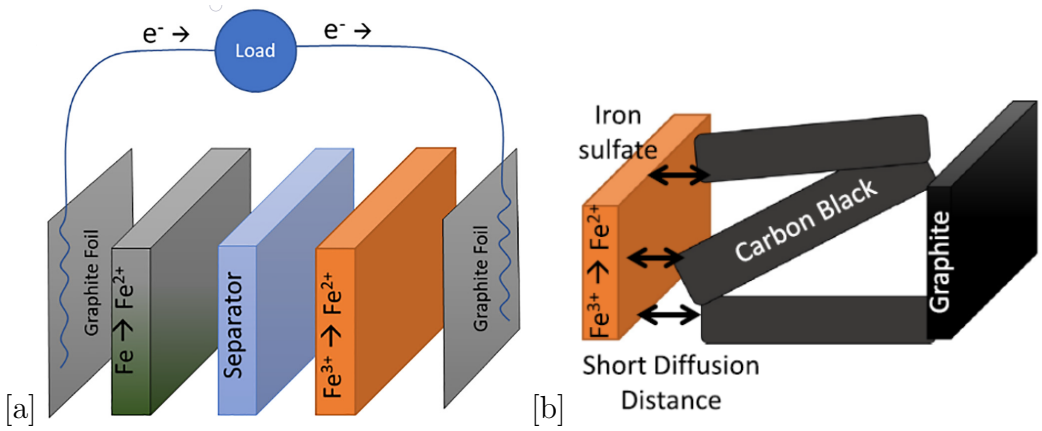

Figure 2.3: (a) Schematic diagram for open-source all-iron battery, (b) The diagram depicts the hypothetical effect of conductive carbon on shortening diffusion distance[17].

anode, describes in chemical reaction 2.2 as follows:

$$\begin{aligned} &\text{at anode:} Fe \rightarrow Fe^{2+} + 2e^{-} \\ &\text{at cathode :} e^{-} + Fe^{3+} \rightarrow Fe^{2+} \end{aligned} \tag{2.2}$$

To maintain a neutral electrical charge, a separator membrane permits positive ions to pass through. According to the result of this paper, the final battery may be used as a reference for the sample cells in this thesis, as it is easy to manufacture with sufficiently abundant materials and can still function well (in terms of capacity) even after operating for more than 1000 cycles. Furthermore, we employ electrical impedance spectroscopy (EIS) to acquire information about the battery's electrochemical system in order to analyze the performance of the batteries we manufacture. This procedure is used on every new battery to assess the battery's initial performance before it is used in this research.

2.2 RFB Testing

Electrochemical Impedance Spectroscopy (EIS) is frequently utilized to study different characteristics and degradation events in electrochemical systems[18]. EIS measures the electrical resistance (impedance) of the electrochemical cell by utilizing a symmetric alternating current (AC) signal over wide-ranging frequencies. It is used to assess electrodes, interfaces, and material characteristics[19] by measuring polarization and ohmic losses associated with an electrochemical interphase or cell[20].

For RFB, EIS provides information regarding kinetics in batteries, such as diffusion

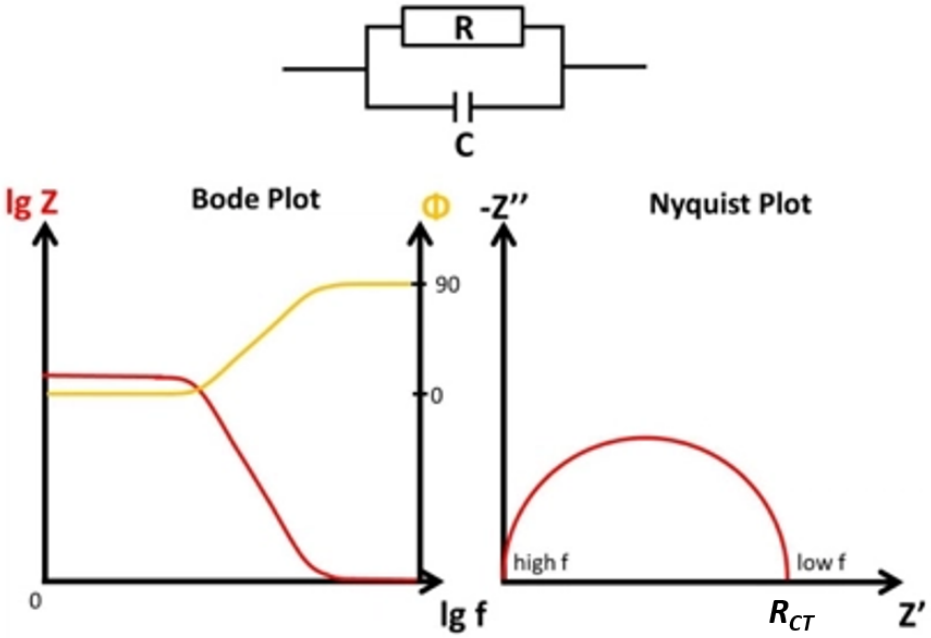

Figure 2.4: An ideal impedance based on RC paralel circuit[21]

processes or charge-transfer reaction dynamics in the electrodes[22]. EIS results in two informations depicted in two plots, Nyquist and Bode plots as shown in Figure 2.4. The Nyquist plot, describes a response of impedance of an equivalent circuit (consists of simple parts such as resistors and capacitors in parallel), which is quite similar to the real functioning system in the cell, determined by using Eq.2.3 for resistor and capacitor, respectively. The horizontal axis represents the real impedance of the resistor and describes the resistance for the electron to change the phase. The vertical axis for the imaginary impedance of the capacitor represents the electrochemical double layer which can only store charge. The capacitor impedance will be very low at high frequencies, and the majority of the current will flow through the capacitor. As the frequency decreases, the impedance of the capacitor increases, and a greater proportion of the current flows through the resistor. When the resistor conducts the majority of the current, the total imaginary resistance Z" decreases as the real part Z' increases. In this case, an ideal capacitor connected in parallel with a resistor forms a semicircle.

$$\begin{aligned} Z_R &= R \\ Z_C &= \frac{1}{j\omega C} \end{aligned} \tag{2.3}$$

The Bode plot is similar to Nyquist plot, but with a precise frequency (or phase, magnitude) axis; hence small impedances in the presence of large impedances can be

identified clearly. This plot depicts the exciting frequencies within an electrochemical system under investigation.

An alternate method for performing the EIS is to use square-wave electrical pulses to measure the electrical characteristics of the material which uses time-domain analysis and has the advantage of measuring the frequency characteristics of the impedance at the same time[23]. Using a pulse wave means that for a predetermined duration, the battery will receive electrical pulses with an ON period (constant voltage) and an OFF period (when the electrode does not draw current from the power supply). Observing the electrical response of the current behavior to a constant voltage can also reveal information about battery performance.

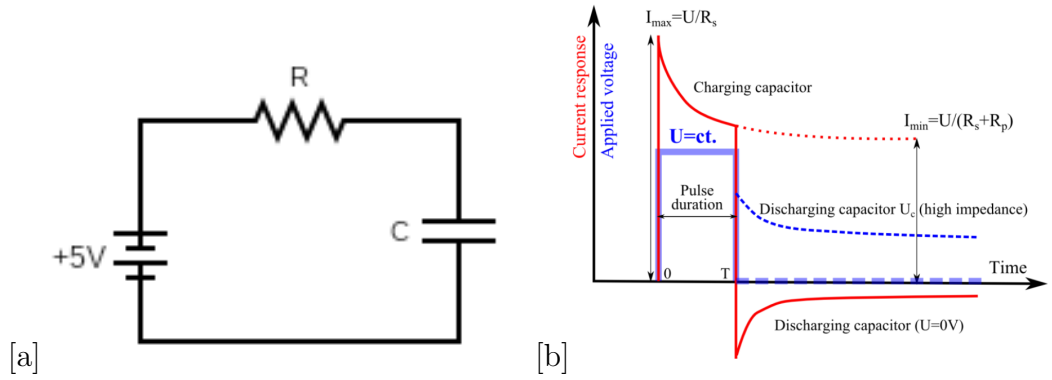

Figure 2.5: (a) A circuit build from resistor and capacitor in series, (b) Current response when a constant voltage (pulse signal, U) applied[23]. During charging, I_{max} is the maximum current at $t = 0$, which decrease to I_{min} at $t = \infty$.

Figure 2.5a depicts an RC (resistor-capacitor) circuit in series which similar with the actual system of our battery cell. The currents flow through a resistor when it is connected to a power supply. According to the Eq.2.4, current is defined as the number of charges, dQ, flow over time (dt) in a close circuit. The current response to a constant voltage will decrease exponentially over time as shown in Figure 2.5b which corresponds to the equation Eq.2.5 where $\tau = RC$.

$$I(t) = \frac{dQ}{dt} \tag{2.4}$$

$$I(t) = I_0.e^{\frac{t}{\tau}} \tag{2.5}$$

This result demonstrates the ideal characteristic of current response when a pulse-wave applied to the battery. In our battery cell, we can also use this characteristic to determine how conductive our battery is, which related to the movement of ions between two electrodes at a particular period.

Electric Double Layer (EDL)

An object's surface develops a structure known as an electric double layer (EDL) when it is exposed to fluid. The two parallel charge layers that surround the object are referred to as the EDL. Ions that have been chemically adsorbed onto the object form the first layer (the surface charge), which can be positive or negative. Ions from the second layer screen the first layer electrically by being drawn to the surface charge by the Coulomb force. This second layer is composed of free ions that move in the fluid under the effect of electric attraction and thermal motion, called the "diffuse layer". EDLs are useful for observing the electrochemical behavior of electrodes. The process of EDLs being formed is shown in Figure 2.6, where electrons and holes are electrically attracted, generating a state between the solid electrode and electrolyte. The EDL stores charge in seconds through an electric double layer created by ions adhering to the surface of an activated carbon electrode.

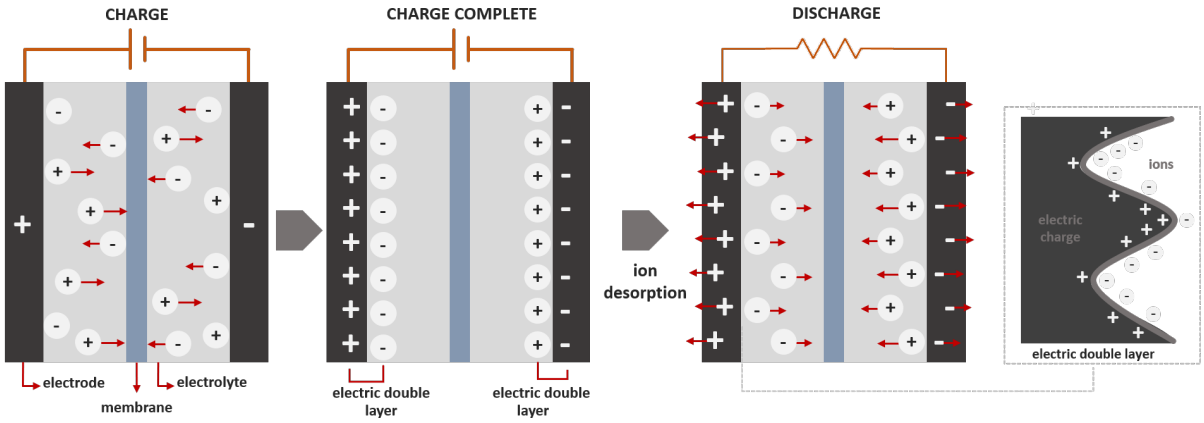

Figure 2.6: The formation of electric double layers during the charging process.

2.3 RFB Monitoring Technique

Microscopy technique is a dynamic and ever-changing tool for probing batteries[24]. In this subchapter, we discuss the Interferometric Scattering (iSCAT) Microscopy which will be used as our main method in monitoring the cell. iSCAT has advantages, notably in terms of its sensitivity to detect ions transfer which involves electrical or structural modifications changes in active material with a simple laboratory-based technique.

2.3.1 Interferometry Scattering Microscpy (iSCAT)

The iSCAT is a fast, label-free, and highly sensitive imaging technique that detects the elastic scattering of visible light by nanoscopic particles[6,25,26] in real time or under actual operating conditions. RFB has never utilized iSCAT as a monitoring tool, however based on previous study[6], this approach can be employed with all types of batteries, particularly to observe the movement or response of ions when subjected to electrical treatment.

For this thesis, the iSCAT will adapt the setup conducted by Cole et al[27] as shown in Figure 2.7a. The incident light (laser diode) is deflected by a beam splitter (partial reflector (PR)) before being focused on the active material in the sample by an objective lens (OBJ) trough back focal plane (BFP). The glass sample's surface will reflect the light (E_r), and the active particles will scatter the light (E_s) to all directions. The OBJ lens will then collect all of the lights and transmit it to the camera via a beam-splitter (PR) with a 50:50 filter of light intensity.

The principal concept in iSCAT is the superposition of electric field of reference beam (E_r) with the elastically scattered electric field (E_s) from active material (see Figure 2.7b). The image intensity then can be calculated as:

$$I_{det} \propto \mid E_r + E_s \mid^2 = \mid E_r \mid^2 + \mid E_s \mid^2 + 2 \mid E_r \mid\mid E_s \mid cos(\Delta\phi) \tag{2.6}$$

with I_{det} is the intensity detected by the detector and $\Delta\phi$ is the relative phase between scatter and reference beam. The cross term in 2.6 (last term) related to the interference of (E_r) and (E_s) which allows for the detection of extremely weak scattering signals, making it sensitive to small changes in the scattering properties of the sample[6,25].

The scattered field (E_s) depends on the polarisability (α) of the active material, $E_s = \eta\alpha E_i$, with E_i is the incident electric field and η is the collection efficiency of detection system. The polarisability of materials denotes the ability to respond to an electric field[28]. Hence, changes in the polarisability of active material during charge/discharge due to electronic changes effect changes in the intensity of scattered light detected by the camera, as E_s is proportional to α.

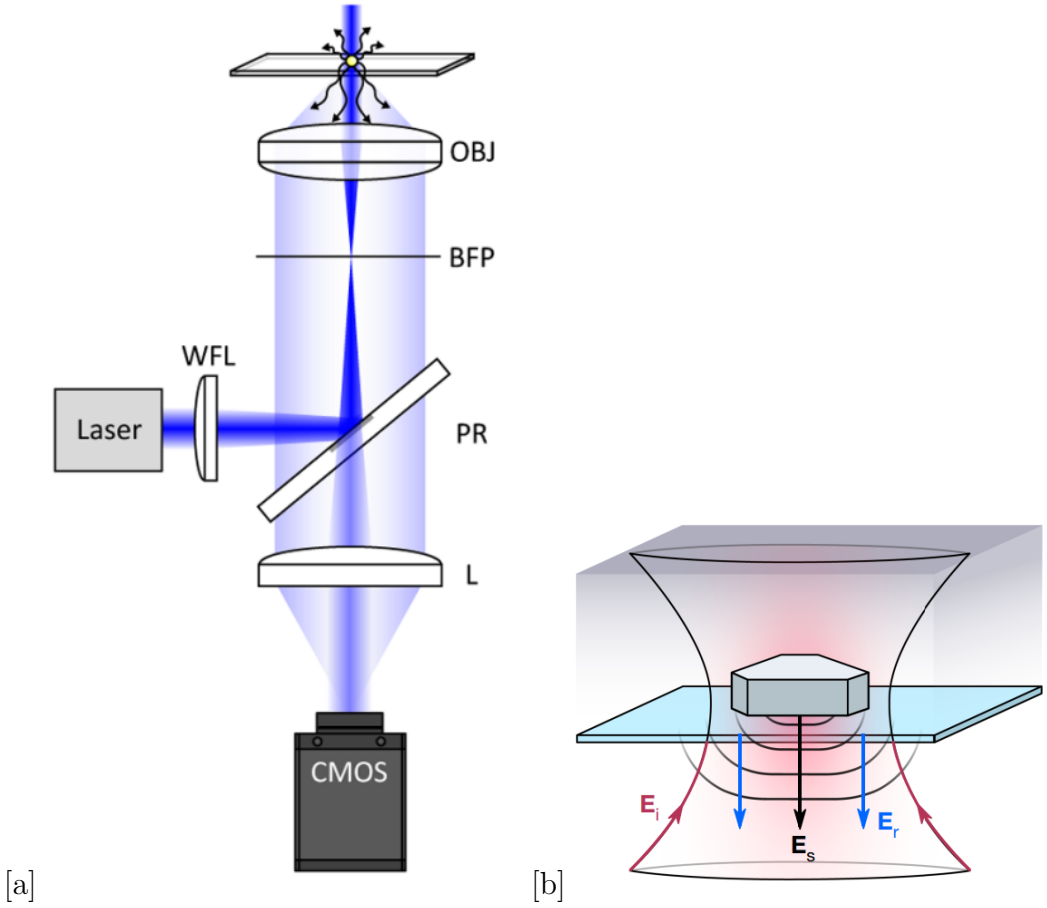

Figure 2.7: (a) A setup for iSCAT that uses a partial beam-splitter to focus light onto an object and pass the reflected light to the camera[27], (b) Schematic diagram of incident light which focused on the sample, reference beam which reflected from the glass or sample surface, and scattered light from the active particle in the sample[6].

2.3.2 Image Processing

Shot-noise limited sensitivity is one of the numerous benefits in interferometric detection[29]. Shot noise or Poisson noise define as the electronic noise that occurs when electrons in an electrical circuit or photons in an optical device are small enough to cause noticeable statistical fluctuations in a measurement[30]. The Signal-to-Noise Ratio (SNR) of an interferometric signal, S, grows as $S = \sqrt{N}$ for shot noise–limited detection, where N is the total number of detected photons. Given that N is proportional to illumination intensity for a given exposure period, the SNR may theoretically be enhanced by simply detecting more photons, either by raising the light source power or the exposure duration. The main challenge is maintaining imaging performance while decreasing noise as the image may be blurry and reduce its contrast. Efficient (digital) background reduction, especially residual substrate signatures, misleading reflections, and lighting inhomogeneities, can be used to counter this[26]. Background correction improves the sensitivity of detection while

also providing more precise localization data[31].

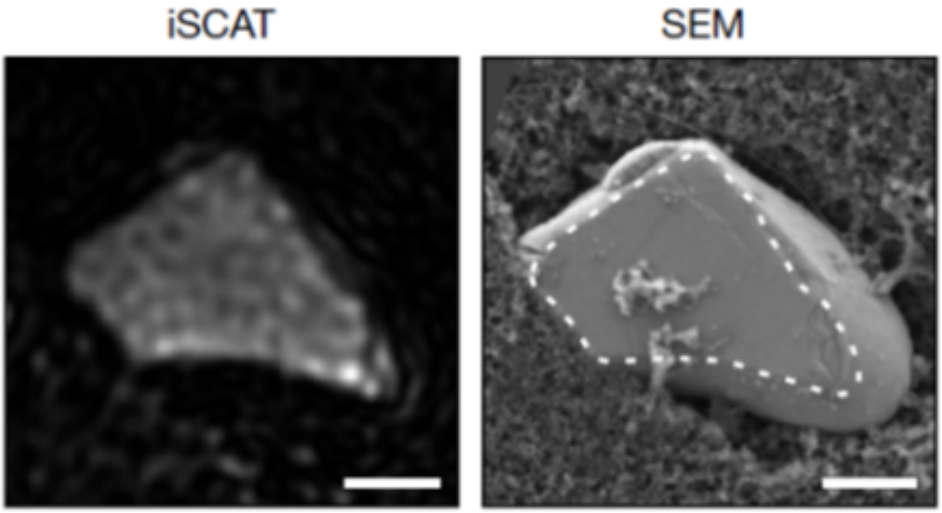

Figure 2.8: Above is sample of Lithium Cobalt (LCO) particle of the active electrode captured by iSCAT microscopy (left) and SEM (right) at 2μm scale bar[6].

Figure 2.8 depicts comparison of image result by iSCAT and Scanning Electron Microscopy (SEM). The contrast between the sample and background in SEM photos is clear, whereas iSCAT produces more fuzzy image. For this thesis, we observe the response of electrochemical activity within the electrode surface due to external modulation. The potential given will be low (∼10-30 mV), resulting in low polarisability of active particle which lead to poor image quality with low signal distribution, low signal contrast, and high noise. Therefore, a background correction technique required for iSCAT in order to provide a contrast image.

Variance Calculation

In image processing, variance measures how much the pixel values in a picture differ from the mean value of all the pixel values. The bigger the variance, the greater the depth of detail in an image. In this experiment, due to the change of potential, the variance of the pixel values may vary. The intensity of an image may be determined using its variance, which can then be used to evaluate distorted images. The variance of the image can be determined using Eq.2.7.

$$\sigma^2 = \frac{\sum_{i=1}^{N} (x_i - \mu)^2}{N} \tag{2.7}$$

with σ^2 is variance of population, N is equal to number of data collection, x_i is ith observation in the population, and μ belongs to the average/mean of population.

Fourier Transforms

Another technique used for background correction in image called Fourier filter. It used a filtering function based on the manipulation of particular frequency components in a signal. While the input image is the equivalent in the spatial domain, the output of the transformation represents the image in the Fourier or frequency domain. Each point in the Fourier domain image corresponds to a specific frequency present in the spatial domain image. It operates by first applying the Fourier transform to the input signal (original image), attenuating, amplifying, or lowering a subset of frequencies, and then applying the inverse Fourier transform to the output (see Figure 2.9a).

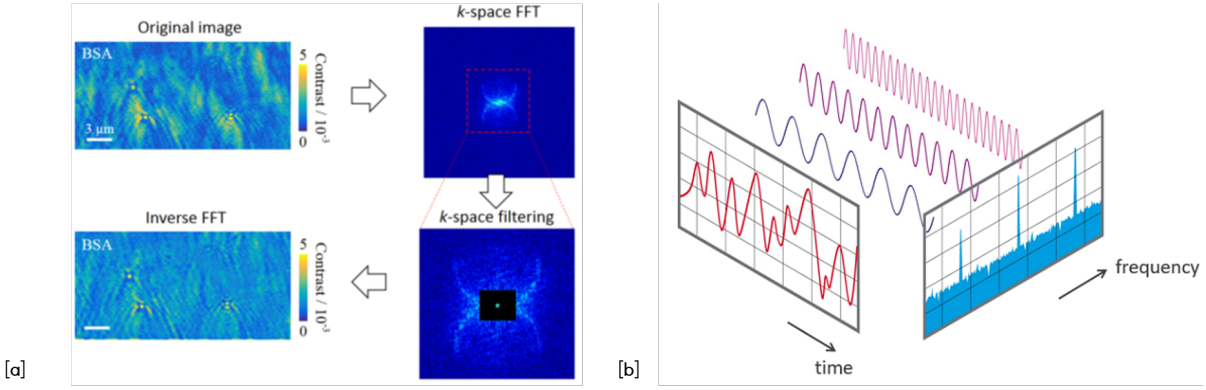

Figure 2.9: (a) View of FFT extracting time-domain signal to frequency domain[32]. (b) Above is the iSCAT image of BSA protein molecules. The original image is transformed to k-space (the frequency domain), showing the rings from interference. The FFT image was then filtered by removing the black mask. After filtering, the image then being inverse back to the space domain results the reducing in background spatial variation[33].

High pass Fourier filter can be used for edge identification in samples by blocking low frequency signal. Band pass Fourier filters can be used to find blobs or edges in images since they only attenuate the frequency beyond the region (band) of interest. Low pass Fourier filter produces smooth noise in the image but fuzzy edges because the high frequencies are blocked. The last filter is better suited in this experiment, the size of the detected particles won't be determined, therefore there won't be a requirement for a contrast edge.

To calculate the signal frequency spectrum on a digital computer, the Discrete Fourier Transform (DFT) technique is used, which turns a time domain signal into a frequency domain signal. The iSCAT method generates an image intensity that is a combination of the reference signal, scatter signal, and shot noise. Because the amplitude of the scatter signal is less dominant, it is difficult to determine if the sample responds to the changes in electric potential, as shown in Figure 2.9b. DFT can aid in this process by transforming

the image intensity performed in time signal $x(n)$ to a frequency signal $F(\omega)$. The formula for the Discrete Fourier Transform (DFT) is as follows:

$$F(\omega) = \sum_{n=0}^{N-1} x(n) e^{\frac{-j2\pi\omega n}{N}} \tag{2.8}$$

Chapter 3

Experimental Section

The experimental setup is divided into three parts, cell preparation, electrical components and optical components as shown in Figure 3.1. For this experiment, to mimic the process occur in RFB, we built a half-cell of all-iron battery, with symmetric electrodes, which the redox reactions occur within the electrolyte placed between two conductive sheets. The sheets are then connected to the electrical circuit which is use as an input signal, for reading the current response also measuring the impedance of the cell. Then, we describe the setup of iSCAT used in the experiment, on how the camera detecting the scattering intensity during the measurement. For image collection and image analysis, we used the Python script explained in the method section. Each material's and instrument's specification as well as Python code are described in the A.

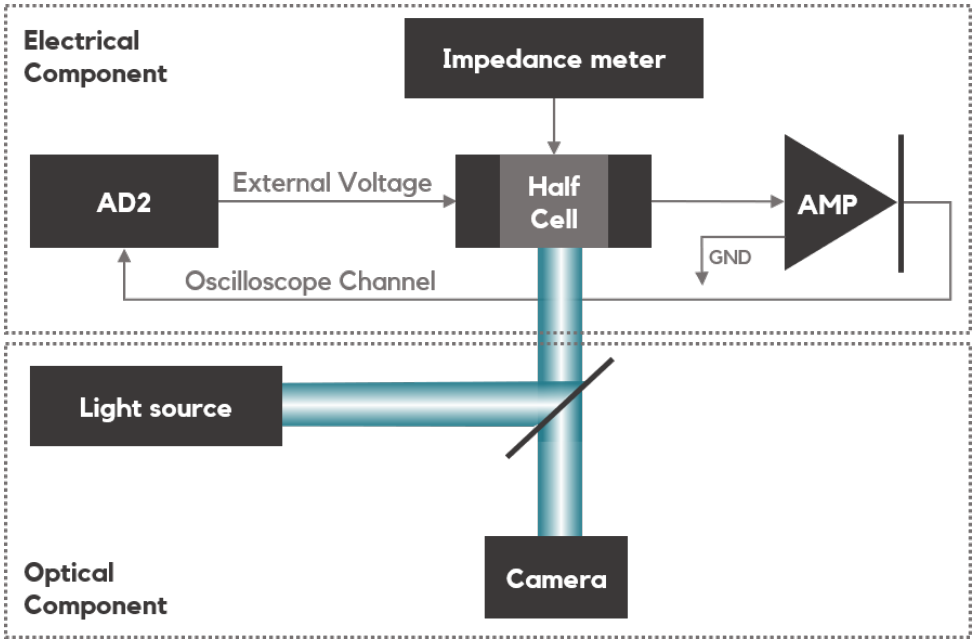

Figure 3.1: Schematic overview of experimental setup with two main parts, electrical and optical components. AD2 stands for Analog Discovery 2 and AMP is lock-in amplifier.

3.1 Cell Preparation

We made a simple half-cell of a battery, with a symmetry electrodes, which allows the exchange of electrolyte throughout the experiment. Figure 3.2 shows the schematic diagram of the half-cell which made by two transparent conductive layers called ITO (Indium Tin Oxide) coatings and between these layers, we made a tunnel from an adhesive double-sided tape with a square window. The ITO layers act as current collectors with copper tapes connecting each layer. To avoid any undesirable scattering contribution, the ITO surface should be free of dust and dirt. The half-cell has window dimensions of around 20 mm, 20 mm, 5 mm for length, width, and height, respectively. We filled the window with carbon felt and three different electrolytes, which are salt, iron (II) chloride ($FeCl_2$) and iron (III) chloride ($FeCl_3$), each used independently. Carbon felt has a good electrical conductivity, make it is possible for ions travel from one ITO layer to another. The thickness of the carbon felt should be as high as the window to ensure both layers connected.

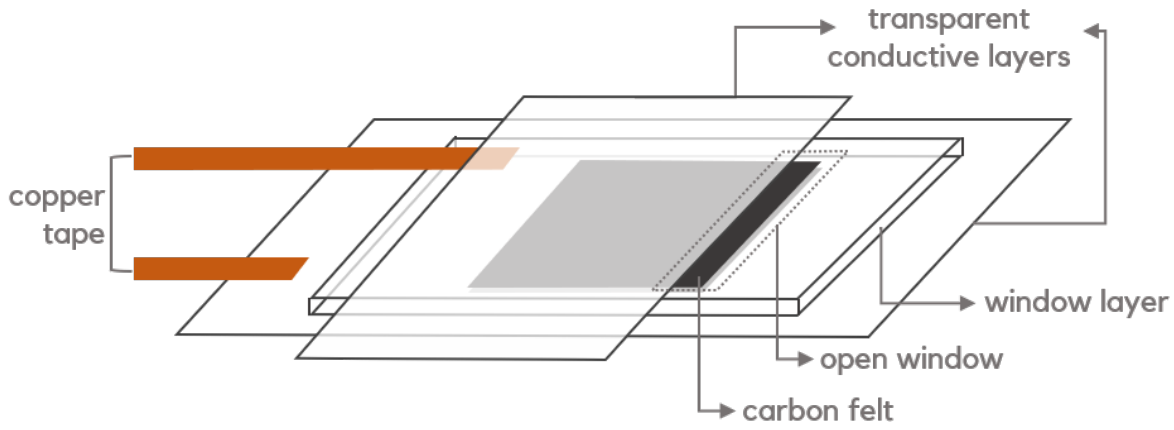

Figure 3.2: A half-cell diagram with symmetric electrodes made from ITO glass and window tunnel for the electrolyte

The ITO layers are very thin and fragile with two different dimensions. The top ITO (made from plastic) is smaller and placed perpendicular to the bottom layer (made from glass), created window tunnel with the thick tape. We used a syringe to fill the window with electrolyte and tissues to empty it through the open window. This method prevents ITO from cracking, as well as electrolyte mixing when refilling the liquids.

3.2 Electrical Component

Figure 3.3 depicts the electronic connections for optical measurement (grey lines) and impedance measurement (orange lines). First, in optical data collection, we used digital wavegenerator-oscilloscope (AD2) as an input-output device for the electric potential that connected in parallel with the half-cell sample and computer. The BNC module is con-

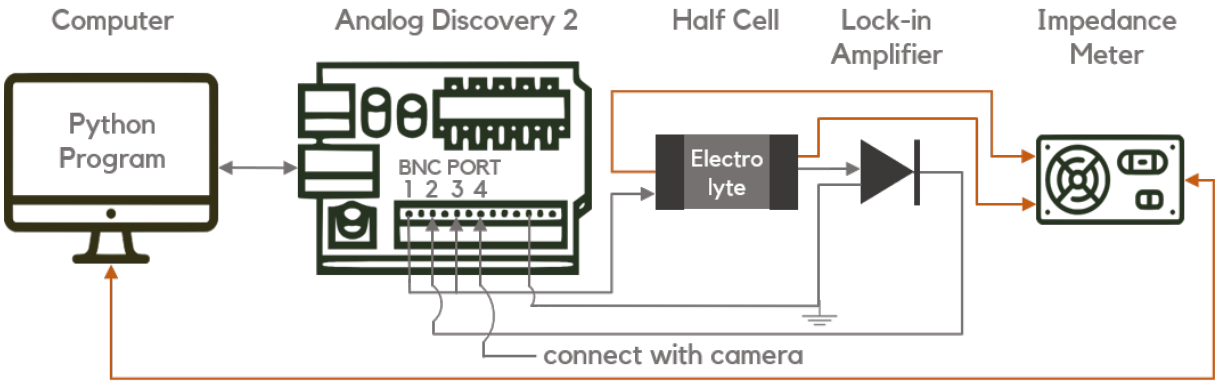

Figure 3.3: Electric configuration setup with grey lines show the connection for input-output potential controller and orange lines for impedance measurement. Arrows pointing in a certain direction show where the signal is coming from and going.

nected to the AD2, use as connection port for wavegenerator (BNC port 1, input signal), oscilloscopes (BNC port 2 and 3, read the input signal from wavegenerator and output signals from the cell , respectively) and camera. The AD2 generates electric potential in the form of DC signal and modulation signal to the cell. As the cell generates a very low output signal, the lock-in amplifier is utilized to amplify it. Second, an impedance meter is used separately with the first circuit for measuring the impedance of the sample. Programs written in Python are used to operate the AD2 and the impedance meter, controlling the overall measurement steps.

3.3 Optical Component

We used a Basler camera as a detector and a fiber laser of ∼405 nm in the optical setup depicted in Figure 3.4 to observe the sample cell from a vertical position. A beam-splitter (BS) that also contains a partial-reflector (PR) mirror and an objective lens (OBJ) is used to guide and gather the lights in order to illuminate the sample. The beam-splitter bends the light to the lens, which then focuses the light into the sample and transmits the light from the lens to the camera by filtering 50% of the light intensity. The black-and-white

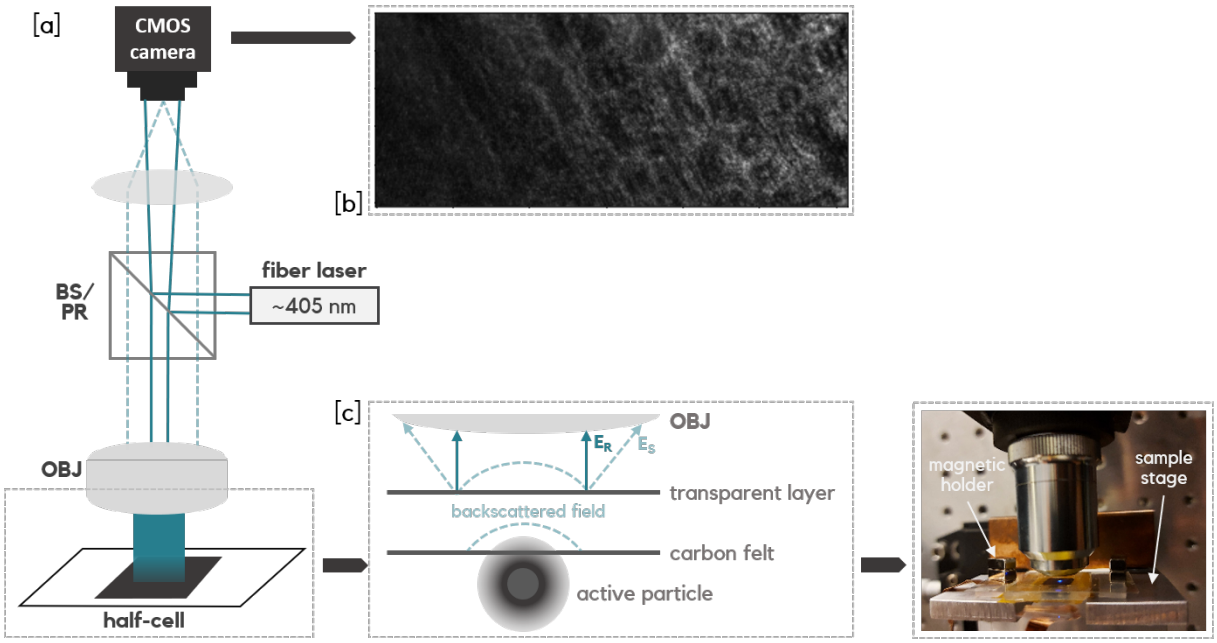

Figure 3.4: (a) Front view of the optical system using the iSCAT technique, showing the sample and camera arranged vertically. The solid green lines show the reference beam path (E_r) and the dash green lines show the scattering beam (E_s) path, (b) The image of the cell captured by the camera in the size of xxx μm, (c) iSCAT setup generates signal from the contribution of E_r, which reflected from the ITO surface and E_s from ions.

camera connects to the BNC port 4 of the AD2, produces an image with resolution of 2048x2048 pixels. The laser as light source is necessary because it generates stable and high-intensity images that are proportionate to the laser's intensity. Then, the sample attached to the sample stage hold by magnets to ensure that the measurement is stable and accurate.

3.4 Method

The experiment is carried out in two stages; conductivity and optical measurement (see Figure 3.5). The first measurement results Nyquist-Bode plot and current response plot to evaluate the electrical conductivity of the cell. The cell must be conductive in order to demonstrate the ions movement between the electrodes. After ensuring that the cell give response to the potential given, then the second stage is conducted which collects a set of images in HDF5 datatype. For each instruments and materials, configuration setup are listed in the Table 3.1.

Preparing sample and microscope.—The electrolyte is poured through the window tunnel (see section 3.1) until it touches both ITO layers. To make sure the ITO surface

Instrument	Parameter
AD2	Combination: 50 mV of modulation signal (sine and pulse wave) and maximum of 500 mV of DC signal Frequency: 1 Hz
Camera	Exposure time: 500 μs Sampling frequency: 70 Hz Binning pixel: 4x4, increase the sensitivity, but reduce the resolution of images Resolution: 616x256 pixels, the resolution is reduced to focus on the region of interest.
Electrolytes concentration	100 mMol of salt, 2 Mol of $FeCl_2$ and 2 Mol of $FeCl_3$
Laser	Fiber laser: 38.6 mA, 0.4 NA, 405 nm
Objective lens	20X magnification

Table 3.1: Table to test captions and labels.

is clear, wipe away any dust or dirt from the sample's surface using a tissue. Put the sample onto the sample stage and hold using the magnets. Turn on the laser and observe the sample through the Basler camera default software, Pylon (the parameters used in the software, such as exposure time and image resolution, must be similar to those implemented in the Python program). The focus of the image is adjusted manually by rotating the focus knobs, which may move the stage in the x-y-z direction to the objective lens. Once the image is in focus, measurements may begin by connecting the two copper tape from the sample with impedance meter or AD2 (see Section 3.2).

Running the measurements.—For impedance measurement, the sample is connected to the impedance meter and the measurement start by running the impedance Python script, which scanned the impedance of the cell from 20 Hz to 1 MHz by applying 20 mV of AC signal. The data is automatically saved in the text document (.txt) format. For current response and optical measurement, the sample is connected to the AD2 and lock-in amplifier. The Python program can be used to measure both measurement objects simultaneously. The written program applying the Python package for the AD2[34] and Basler camera, so it can generates as well as receiving the signal from the cell and the camera. The AD2 generates a combination of modulation signal and DC signal operates at 1 Hz of frequency. The frequency is chosen to ensure that the camera capture ade-

quate number of images during the measurements. The program is designed to perform measurements with and without potential sequentially for 4 cycles. In measurement with potential (ON cycle), the DC signal is increased gradually from -500 mV to 500 mV, step of 100 mV. For each steps, the camera collects 700 data, in the form of array frames, which later called as a dataset. Until the measurement is complete, all frames are recorded in the HDF5 datatype.

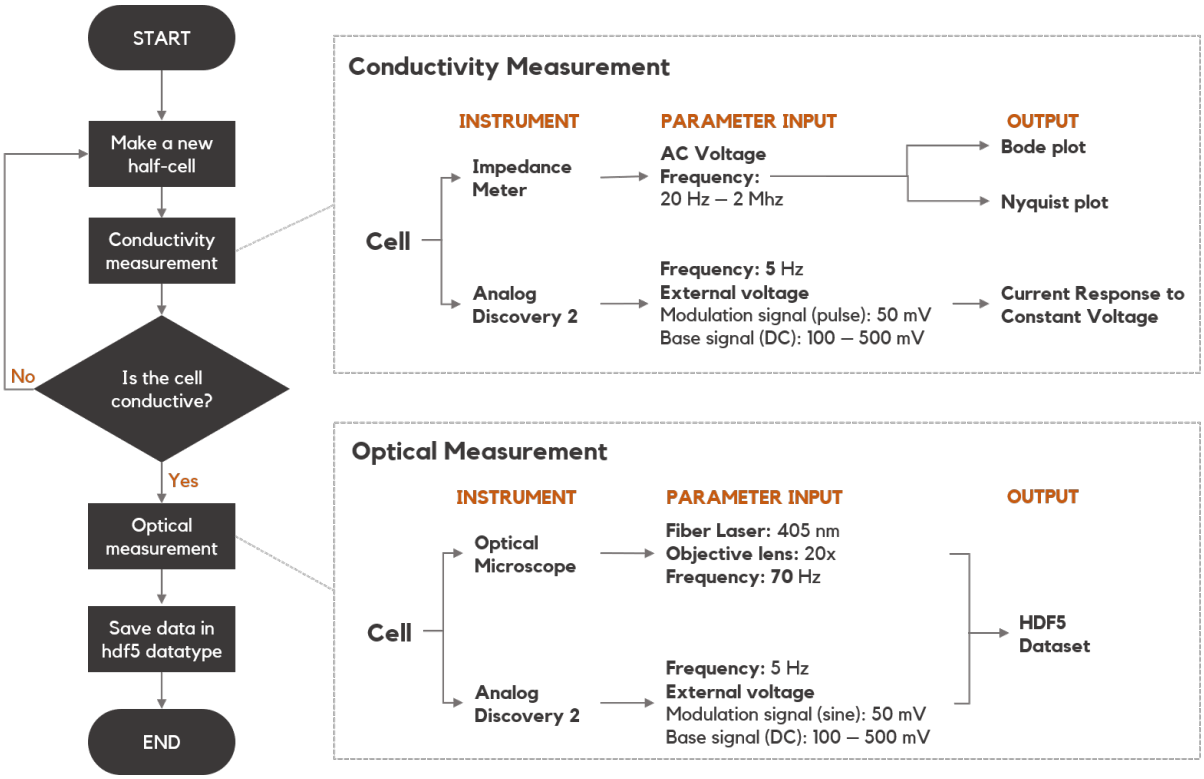

Figure 3.5: Flowchart of the cell measurement, conducted in two steps; conductivity and optical measurement.

Chapter 4

Validation

4.1 LED Measurement

A white LED is used as a sample to characterize the optical setup. The LED is chosen as it can adapt to the applied electric potential and affect both brightness of the LED and the intensity of the captured image. This is an ideal response that we want to observe using the actual cell. The LED is connected to the AD2 (replacing the cell, see Figure 4.1) using parameters below:

- electric potential, combination of: 3-4 V (step 0.1 V) of DC (offset) and 30 mV of modulation signal (sine wave). To light up, a white LED required 2.7 V of minimum voltage.
- modulation frequency: 1 Hz (period = 1 s)
- 2 cycles of measurement (1 cycle = with potential (ON) + no potential applied (OFF))

According to the setting, the camera collects 70 images per 1 s for 50 times, resulting in 700 images/array for each potential called datasets. All of the data and image processing were conducted after the measurement was completed.

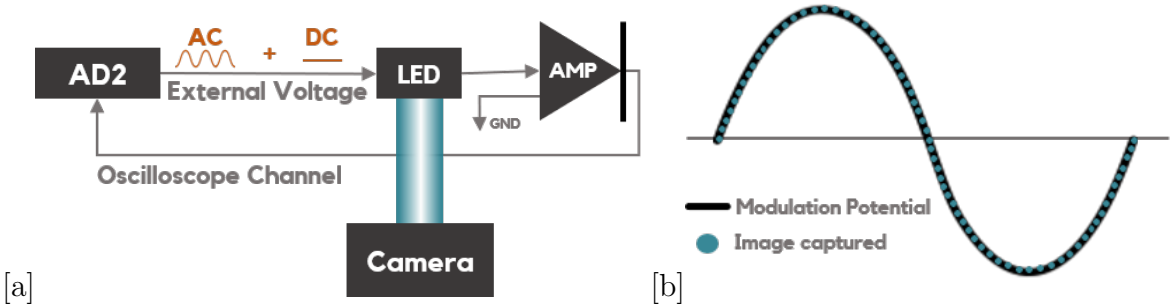

[a] [b]

Figure 4.1: (a) Diagram circuit for LED measurement. The electric potential is the combination of DC (base) and modulation signal (sine wave). The modulating signal was applied to affect the brightness of LED changes periodically, resulting the intensity captured by camera change in certain period (b) Illustration of number of images capturing by camera. It is essential to set the modulating frequency lower than the sampling frequency of the camera, so the images captured will represent parts in the modulating signal. We modulated the signal at 1 Hz while the camera works at 70 Hz, resulting in 70 images captured per 1 second.

4.2 Variance Analysis

The variance of an image is a measure of how much the pixel values differ from the mean value of all the pixel values. The higher the variance, the more detail there is in an image. Figure 4.2 depicts the variance per datasets that occur in 2 cycles (1 cycle occur from 0 to 200 second, the voltage off at 100 to 200 second). When the voltage input is low, the measurement results show a narrow range (close to zero) and widen as the value of the input voltage increases respectively, this indicates that the camera captures the intensity that occurs from the lowest up to the highest resolution. At low voltage, however, the light source only generates intensity within a specific range of resolution.

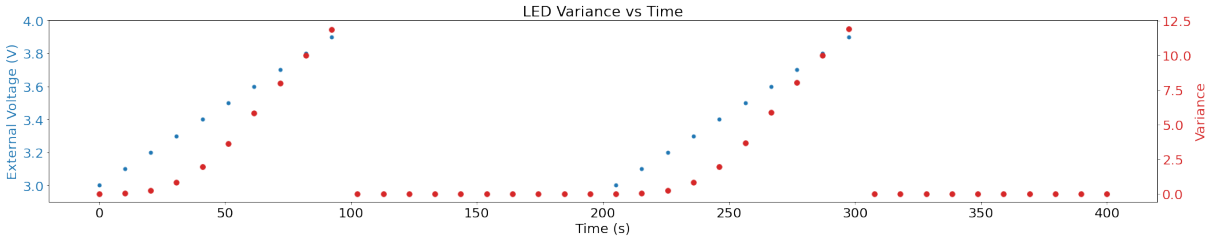

Figure 4.2: LED variance per data set versus time.

The high variance indicates the wide range of intensity values in a data set, which conclude that the camera is able to record changes in intensity from low to high. However, lower voltage (below 3.3 V) show the variance that close to zero, indicating that the intensity shift is very slight, or it can be inferred that the camera is less proficient at detecting light at this voltage.

We also utilize the variance calculation to predict the location of ions in images, which can operate as a background correction for image analysis by providing the intensity trend. Background correction is required to remove or minimize noise captured by the camera during measurement. Figure 4.3a depicts a selection of images from each data set that will be subjected to variance calculations. In image processing, variance can be used to recognize sharp characteristics like edges and categorize into several areas, also suitable for removing noise in image[30].

The variance filtering the low frequency[i] in images, making it easier to evaluate which area of the image is interesting for further examination. The variance was calculated for every 70 images of 700 images, resulting 50 variance images per dataset (Figure 4.3b).

[i]In image processing, frequency refers to the rate at which intensity values fluctuate. Low frequency indicates the intensity of images change gradually or the brightness relatively constant

These images then could be referred to determine the region of interest (ROI) to be observed further. In this experiment, the ROI was manually defined by looking at areas that changed frequently throughout the measurement.

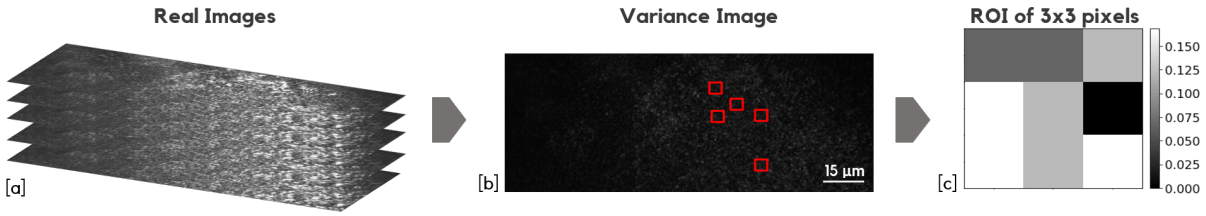

Figure 4.3: The image captured by camera is in the size of 15 μm. Picture (a) illustrates a collection of images in 1 Hz (70 images) that being calculated for variance analysis resulting image in Picture (b). Picture (c) represent one of the 3x3 ROI of the red square.

4.3 Intensity Profile

As mention in measurement setup, two combined electric potential were applied to the sample, DC and modulation signal (sine wave). The modulation was used to examine whether the periodic potential has an impact on the brightness of LED. In order to avoid a non-linear circuit—one in which the parameters voltage, current, and resistance is not constant—it is required to set the modulation lower than the DC voltage.

In order to lessen the impact of noise on the area being observed, a 3x3 pixel of ROI (Figure 4.3c) was used in LED analysis, which then applied to all images. All ROI images then being filter using low-pass Fourier filter to smoothing the image by reducing the difference between the pixel values and the average of the closest pixels (see Figure (show ROI after and before filter)). Then, the intensity of each image is measured by adding the pixel intensity values in each image, which describes the behaviour of the brightness of LED. Plotting the intensity images over time as shown in Figure 4.4 is able to define the intensity profile for the overall measurement. Generally, it clearly seen that the change in potential affected the image intensity for each dataset, since the increase of potential also increases the image intensity. Higher potential also makes the intensity's dynamic range[ii] appear broader. However, there is zero intensity at a voltage of between 3.0 to 3.6 V, indicating that the camera does not capture light despite the increased voltage.

Figure 4.5 depicts the intensity response due to the modulation signal. The lower the potential supplied, the less LED intensity may be captured by the camera. The opposite

[ii]Comparison of the highest and lowest light intensities that can be measured

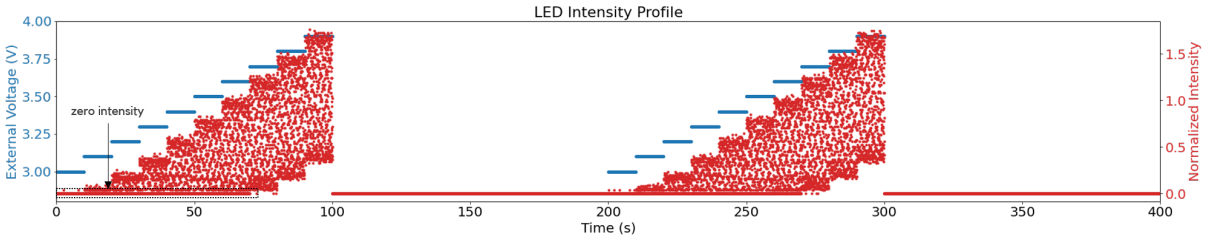

Figure 4.4: The blue dots represent the peak-to-peak amplitude summation of DC and modulation signals, while the red dots are the normalised of integrated intensity of 28.000 images.

is also true: the more intensity, the more the camera record (seen from the data points for one sine wave). At the 3.0 V dataset, the camera captured zero intensities almost for all data points when the LED was blinked with low intensity. Data points with zero values decreased from 3.1V to 3.5V and began to respond stably from 3.6V to 3.9V voltage. The results show that images captured during measurement started to follow the trend of modulation amplitude as the potential gets higher.

In this experiments, the intensity profile can show one of the characteristics of the ions during operation, namely reversibility. A good reversibility can be interpreted by a proportional change in the intensity value to the change in electric potential after many cycles.

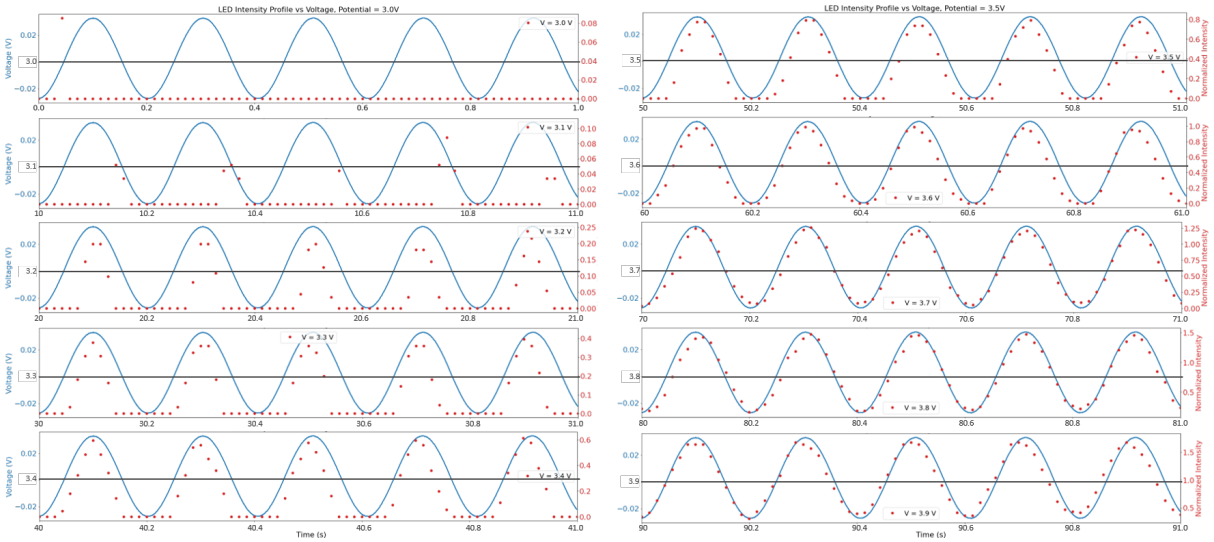

Figure 4.5: Oscillation of LED's brightness (red dot) for 0.3mV of modulating signal (blue line).

4.4 FFT Signal Analysis

It is essential to ensure that the intensity periodicity corresponds to the modulation period, which is at 1 seconds (1 Hz). The Fast Fourier Transform (FFT) was then utilized to extract the frequency of the intensity profile, as it can effectively calculate each frequency component of time-varying signals.

We applied several modulation signal amplitudes for LED measurement to evaluate the lowest potential the system can detect. Figure 4.6 depicts the FFT graphs of; 50 mV, 30 mV, 10 mV, 5 mV, 3 mV and 1 mV. The brightness of an LED responds favourably to potential changes at modulation greater than 5 mV, and graphs using these potentials show a peak at a frequency of 1 Hz, indicating that the signal received from LED has a bigger amplitude than the noise. On the other hand, low modulation signal ($\leq$ 5 mV) makes the LED's intensity less dominating than noise, making it impossible for the system to detect periodic changes in intensity.

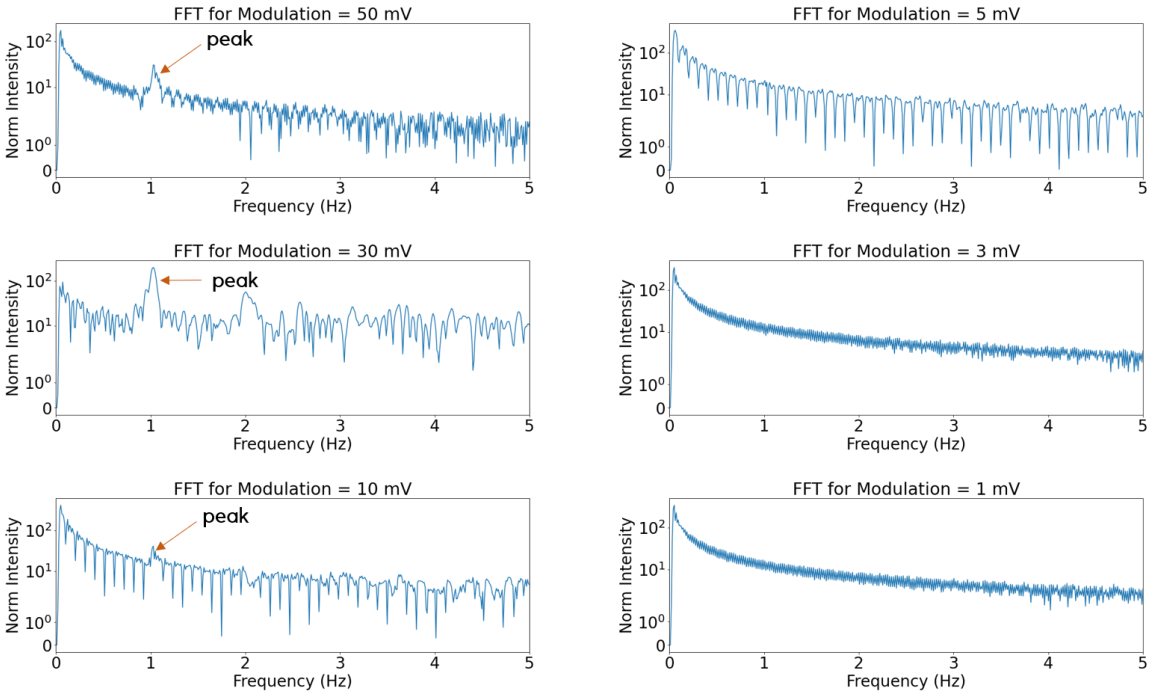

Figure 4.6: The FFT of LED intensity profile for different amplitude of modulation

These results show that the intensity of the dataset changed periodically following the modulation voltage at 1 Hz, indicating that the modulation signal affects the brightness of the LED. According to these results, we can conclude that the measurement system and analysis process is sufficient for the half-cell experiment, when a potential greater than 5 mV is applied.

Chapter 5

Result

The main goal in this experiment is to investigate the response of ions in an all-iron half-cell due to external potential as a result of an electrochemical reaction when the cell is in operation. As a first step in the study, we analyze the conductivity of the battery cell to identify any moving ions during cycles. Then, we investigate the image collections to observe ion response by comparing image intensity to different parameters such as voltage and frequency. In this experiment, we examined three half-cell samples containing various electrolytes: NaCl, $FeCl_2$, and $FeCl_3$, with the last two electrolyte were commonly used to build an all-iron battery.

5.1 Cell Analysis

When connected to the potential, the electrochemical system in the cells is modelled as an equivalent circuit of resistor-capacitor (RC) circuit due to the mechanism called electric double layer (EDL), so Figure 2.4 and 2.5 are used as a reference for the EIS and current response results, which show that ion transfer between electrodes occurs within the cell.

5.1.1 NaCl

The current response of a NaCl cell are depicted in Figure 5.1a (no carbon felt) and Figure 5.1d (with carbon felt). The red lines show the input of pulse signal at a frequency of 1 Hz, while the blue lines is the output signal of current response. In comparison to NaCl with carbon felt, a NaCl cell without carbon felt requires more time for the current to decay, approximately 0.1 s (see time decay, Eq.2.5) from I_{max} to I_{min}, indicated that the EDL is formed longer without the carbon felt, as well as the ions movement.

The EIS results show that the cell is conductive when seen from Figure 5.1(b-c, e-f). The Nyquist plots create a semicircle representing charge transfer occurs in the battery. In addition, it is clearly seen from comparing the Nyquist plots before and after cycle (Figure 5.1 c and f), that the charge transfer (R_{CT}, see Figure 2.4) in a cell is decreasing which

indicating there is a change in the capacity of capacitor due to many cycles of operation. In the Bode plot, the capacitor's impedance will be very low at high frequencies, and most of the current will pass through it. As the frequency decreases, the capacitor's impedance rises, and more current passes through the resistor. In general, the impedance generated by the cell with felt is greater than that produced by the cell without felt in EIS plots.

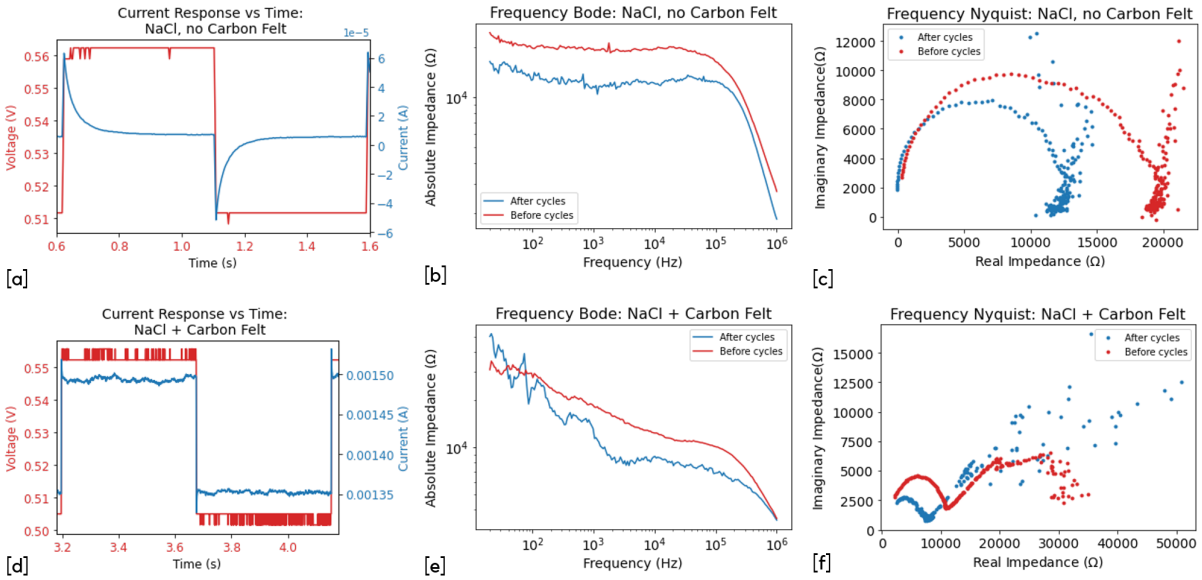

Figure 5.1: (a-c)Current response, Bode and Nyquist plot for NaCl without Carbon felt; before (red) and after (blue) cycles, (d-f) with Carbon felt.

5.1.2 Iron II Chloride ($FeCl_2$)

The current repsonse of the cell with $FeCl_2$ as the electrolyte is depicted in Figure 5.2(a,d), without and with the carbon felt within the window layer, respectively. The graphs show a trend wherein the cell with carbon felt deteriorate more rapidly than the cell without felt, almost equivalent to the cell with NaCl. Both of these graphs have a rather quick decay time, but the combined graph still depicts ion mobility within the cell. Experimentally, this might be due to the ease with which the electrolyte solution precipitates during the measurement and causing the concentration of ions in the solution to decrease. Although both of these graphs have a rather rapid decay time, they nonetheless demonstrate ion movement within the cell.

In the EIS test, the impedance of the cell at low frequency without felt is in the order of 10^5 Ω, but the impedance of the cell with felt is significantly less, approximately $2x10^3$ Ω. According to the Bode plot, Figure 5.2(b,e), the two cell conditions match the predicted circumstances, with a modest impedance response at high frequencies and a

strong impedance response when the frequency is dropped. For the Nyquist plot, the cell without carbon felt (Figure 5.2c) responds in a manner consistent with the characteristics of the RC circuit, which formed a semi-circle when subjected to a frequency change. The graph in Figure 5.2f, however, does not depict the properties of the RC circuit in a cell containing carbon felt as it does not produce the expected semi-circle. Nevertheless, these cells is deemed capable of flowing ions, from one electrode to another, even in a very short period of time.

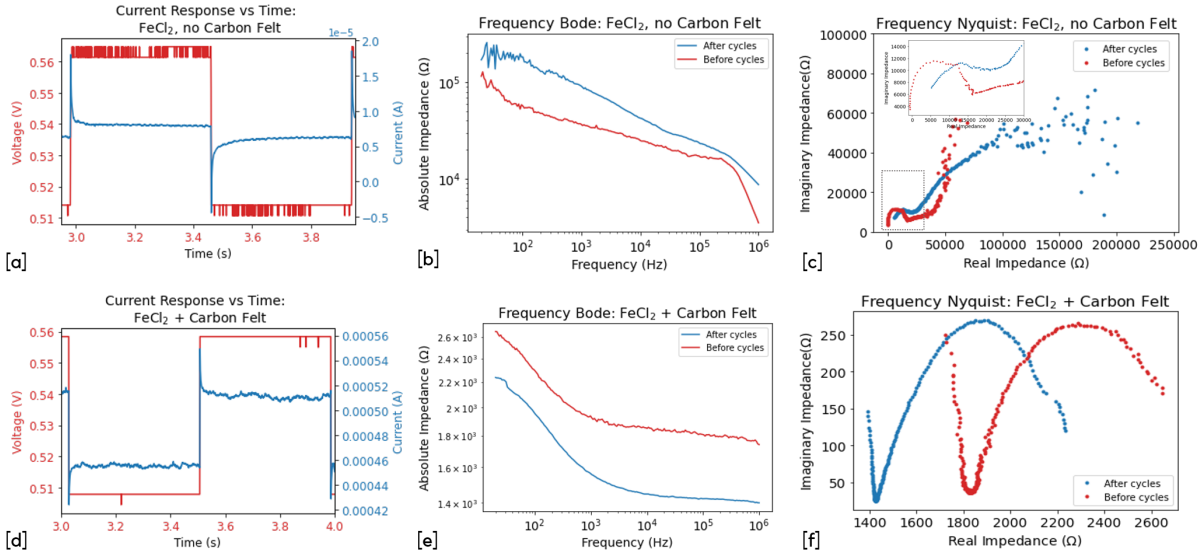

Figure 5.2: (a-c)Current response, Bode and Nyquist plot for $FeCl_2$ without Carbon felt; before (red line) and after (blue line) cycles, (d-f) with Carbon felt.

5.1.3 Iron III Chloride ($FeCl_3$)

A cell with $FeCl_3$ electrolyte is also tested for conductivity. Figure 5.3(a,d) show the current response for the cell without and with carbon felt, respectively. From I_{max} to I_{min} for both plots, there is a steep decline, showing that the decay time is quite rapid, compared to other electrolytes. This circumstance indicates that ion movement in this cell only happens over a relatively brief period of time before eventually reaching a saturation state at I_{min}.

The EIS measurement results are next examined; the Bode plots provide a curve that matches to the RC characteristics, although both graphs reveal relatively high impedance values ($\sim 10^6\ \Omega$) when applied at low frequencies once the cycle procedure is finished. Then, the Nyquist plots show a curve that is consistent with the typical RC circuit, where a semi-circle is generated to signify a transfer of charge within the two cells. R_{CT} likewise

undergoes a change with a higher impedance value once the cycle is finished. The cell with carbon felt is obviously quite far away from the early R_{CT}, suggesting that the cell is allowing less charge to flow.

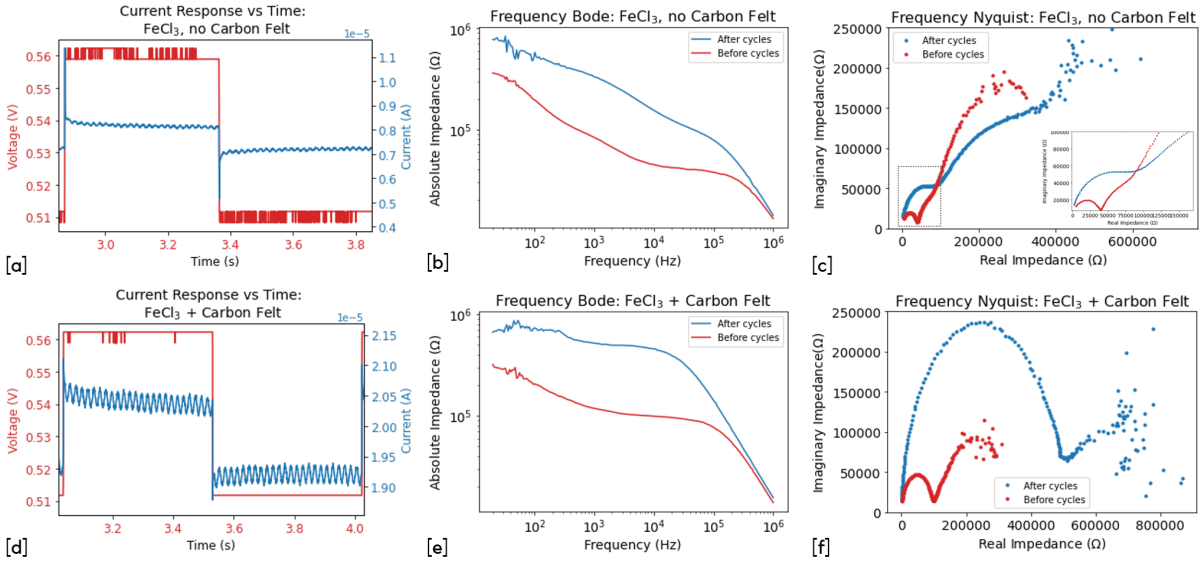

Figure 5.3: (a-c)Current response, Bode and Nyquist plot for $FeCl_3$ without Carbon felt; before (red) and after (blue) cycles, (d-f) with Carbon felt.

To conclude, the three cells show electrochemical activity in the cell when given an input signal in the form of a pulse wave (representing a constant voltage) and different frequencies. This activity is an indication of the presence of ions moving from one electrode to another.

5.2 Images Analysis

The active particles (ions) scattered the light weakly, making them difficult to detect by the camera and generating image noise. The image filter technique must be applied to smooth out the noise before being used in the analysis. First, we applied the variance calculation to the set of images in order to determine the region of interest (ROI). Then, after each ROI image was filtered using a low pass Fourier filter, the integrated intensity of each ROI image was calculated. Lastly, we used the Fast Fourier Transform (FFT) to determine the oscillation frequency of the ions. At the end of the analysis, we can predict whether the ions are responding to the electric potential given. Only the results of intensity against time graphs, contrasts between modulation signals and intensities, and conversions from time-domain signals to frequency-domain signals are displayed in

this section. The phases in the ROI selection procedure are quite similar to those in Figure 4.3(b-c).

5.2.1 NaCl

The conductivity tests indicate that the NaCl cells could engage in electrochemical processes when the electrodes are connected to a voltage. However, when compared to optical observations, the results obtained do not match those of measurements done with an LED. Figure 5.4(a-middle) depicts the intensity profile of NaCl cell without carbon felt, with the blue line serves as a reference point and indicates voltage while the red line shows the image's normalized intensity plotted against time. In this graph, the red line seems to oscillate throughout measurement, despite the fact that the oscillation represented is unaffected by the input modulation voltage. When we zoom in on one of the datasets (in this case, the data set for 0.3 V), as shown in Figure 5.4(a-top), we can clearly see that the intensity of each image is not a function of the applied modulation voltage. As a consequence, there is no significant peak showing in Figure 5.4(a-bottom), at 1 Hz when we applied the FFT to convert each dataset.

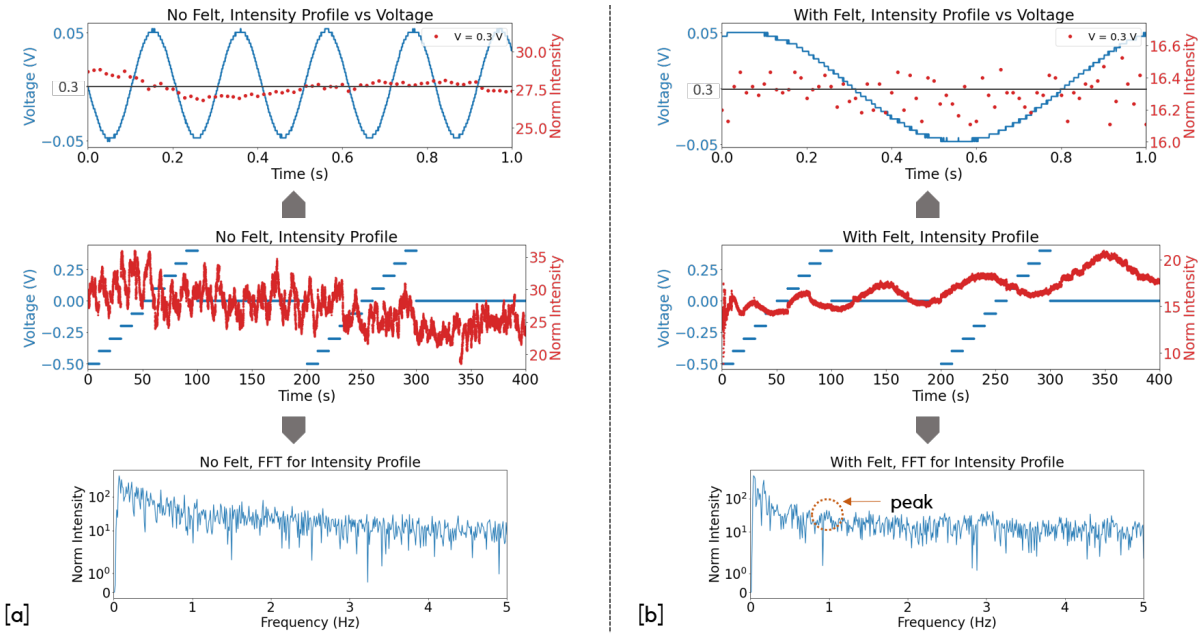

Figure 5.4: Image analysis for NaCl cell: a. without carbon felt, b. with carbon felt

The NaCl cell containing carbon felt experienced the similar phenomenon, as demonstrated by the intensity profile in Figure 5.4(b-middle). It is immediately apparent that each image's intensity oscillates, yet the input voltage has no bearing on this oscillation.

In Figure 5.4(b-top), the intensity of each picture is likewise shown to spread out, making it impossible to detect the correlation between voltage changes and intensity variations. However, it's noteworthy to note that when the data is translated to the frequency domain, a peak at a frequency of 1 Hz appears to be somewhat more prominent. This peak, as shown in Figure 5.4(b-bottom) suggests that ions may respond when input is provided at a voltage of 0.3 V. Unfortunately, no peak at that frequency can be seen when analyzing different datasets.

5.2.2 Iron II Chloride

The $FeCl_2$ cells also demonstrates ion mobility when observed from the conductivity test. According to the optical findings in Figure 5.5, the FFT transformation does not appear to have a dominating peak at 1 Hz, whether in cells that utilize carbon felt or not. Although the intensity profiles of each cell appears to fluctuate, it is not a function of the input voltage. As shown in Figure 5.5(a-b, top) that the image intensity appears to be constant and does not follow changes in voltage.

Referring back to the results of the current-voltage response (see Figure 5.2(a,d)), the decay period of the cells is rather quick, which demonstrates that the concentration of ions in the ROI is decreasing, hence the camera no longer captured the response from ions.

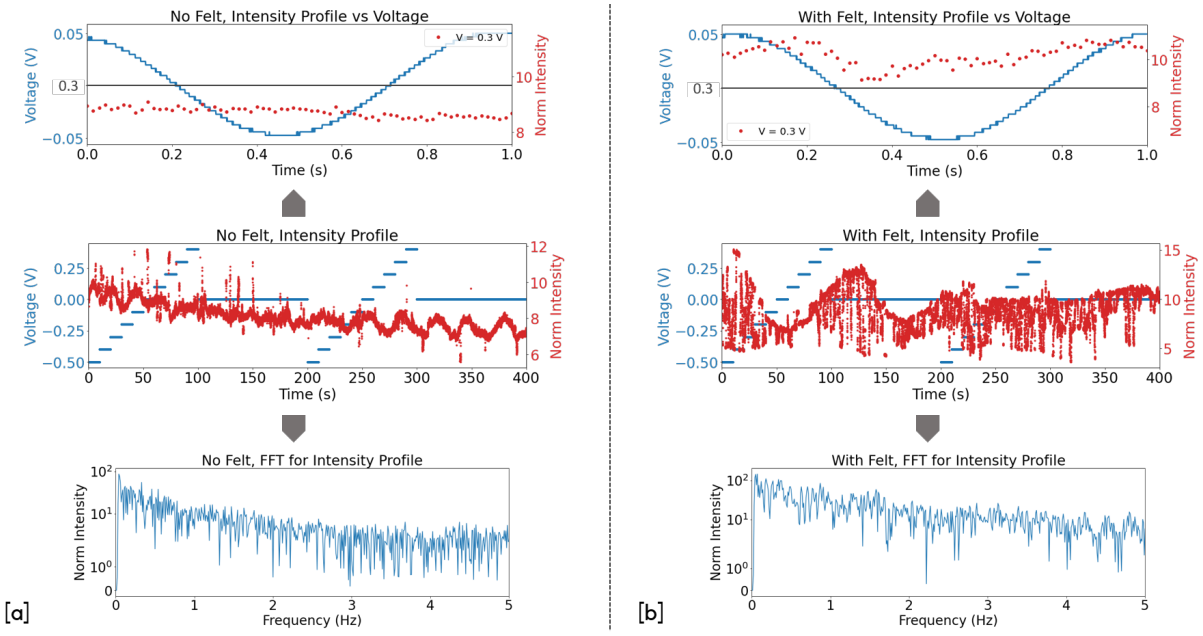

Figure 5.5: Image analysis for $FeCl_2$ cell: a. without carbon felt, b. with carbon felt

5.2.3 Iron III Chloride

According to conductivity tests, the $FeCl_3$ cell may trigger the electrochemical process (when coupled to a voltage), causing the ions to flow through the cycles. Optically, the pictures produced by this cell measurement exhibit a variety of outcomes, with the ion response being unable to discern by image processing. The intensity profile in Figure 5.6(a-middle), which generated by cells without carbon felt, produces fairly distinctive results, with the intensity fluctuating throughout the initial ON cycle and then becoming consistent while entering the OFF cycle. However, when it re-enters the ON cycle, it remains steady before ultimately moving downwards till the measurement ends. Furthermore, if we examine at the intensity distribution across the modulation voltage, as shown in Figure 5.6(a-top), the intensities are unaffected by voltage changes since they are distributed randomly. This graph, when processed using FFT, does not reveal a strong signal amplitude at 1 Hz. The dominance of noise appears to be greater in Figure 5.6(a-bottom), which depicts the frequency domain for the 0.3V dataset, making the amplitude of the modulation signal less noticeable.

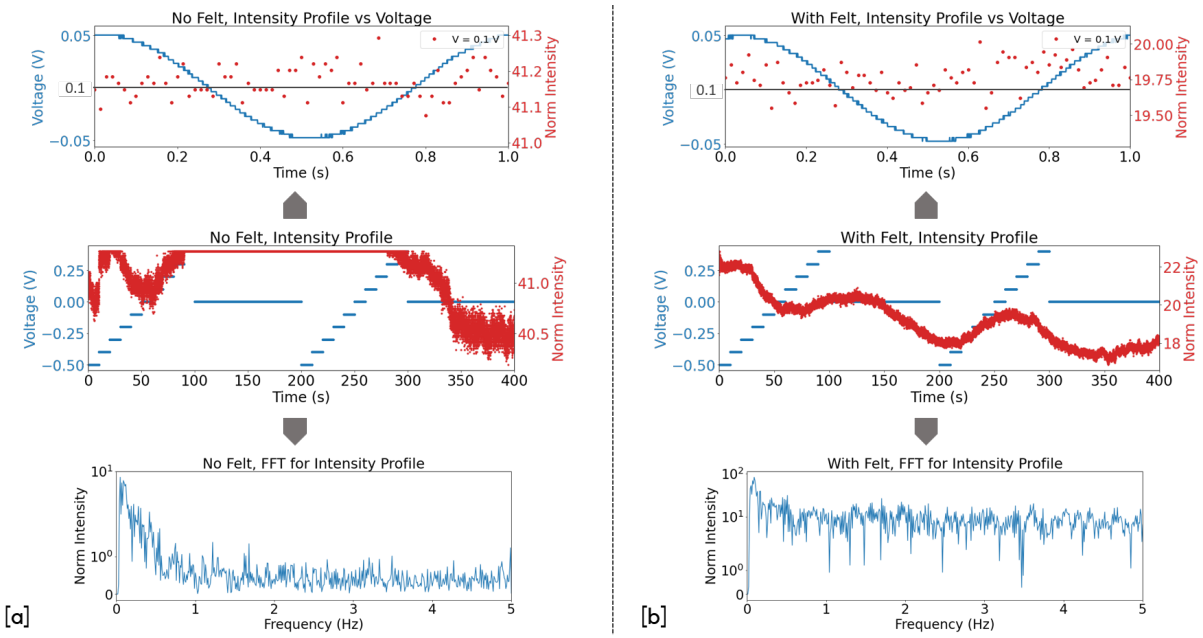

Figure 5.6: Image analysis for $FeCl_3$ cell: a. without carbon felt, b. with carbon felt

Figure 5.6(b-middle) exhibits the intensity profile of a carbon felt cell and shows a decreasing-amplitude oscillation that lasts until the measurement is finished. However, if the spread of the intensity of the modulation signal is examined, as shown in Figure 5.6(b-top), it can be concluded that the intensity is independent of the input voltage. It

is clear that fluctuations in image intensity are not caused by voltage changes because there was no dominant signal at 1 Hz in the FFT transformation, which illustrated in Figure 5.6(b-bottom).

In general, for all cells, since the intensity of the images is independent of changes in voltage, the optical results often do not display a pattern corresponding to the LED measurement. Consequently, when the signal from the time domain is translated to the frequency domain, no dominating signal is discovered at 1 Hz.

Chapter 6

Discussion

In this chapter we will discuss the results obtained from chapter 5, and the possibilities reasons and suggestions for further research.

6.1 Cell, carbon felt, and electrolytes

The measuring technique is hindered by a number of challenges that arise throughout the cell manufacturing process. The first problem is that the substance from the ITO glass conductive layer is very thin and fragile, which leads to numerous fractures when utilized frequently. The potential between the conductive layers and the ITO layer may become disconnected due to of cracks in the ITO layer. In order to make sure that all of the components are linked correctly, a new cell is required for each measurement. The second obstacle is ensuring that the two conductive layers will be connected when the electrolyte solution is added. Due to the fact that the two layers are only joined by tape, there is a chance that the tape will fall off during measurement, leading to an unstable connection between the two layers. When carbon felt is inserted, which is somewhat thicker than the window layer, this configuration made worse. Layer connections are getting harder to connect and come to be one of the factors contributing to the cell's unstable voltage. The third problem is the $FeCl_2$ solution which easily precipitates. In the experiment, it causes the solution to become less conductive, which might be owing to a drop in ion concentration. Furthermore, because silt accumulates in the layer that will be seen by the camera, it might obstruct the object area from being observed. For $FeCl_3$, despite the absence of precipitation, the conductivity of the solution was reduced after a few days. As a result, taking measurements shortly after the solution is created will be more effective.

In RFBs, carbon felt plays a significant role as a conductive substance that may speed up ion movement from one electrode to another. This experiment shows that using carbon felt increases the amount of current flowing in the cell by about ten times, as shown by the current response (see Figure 5.1, 5.2, 5.3 part (a,d)).

6.2 Response of intensity to the potential changes

In this study, we hypothesize that the intensity of images fluctuates proportionally to changes in electric potential, which indicate the response of active particles (ions).
According to the results in chapter 5, the ion's response is not detectable optically through the recorded images. When the intensity profile in the time domain is translated to the frequency domain, there is no prominent peak at the input frequency. We looked at several things that may have impacted these findings:

- When the conductivity test results are evaluated, practically every cell shows evidence of ion movement, assessed using graphs of current response, Nyquist, and Bode plots. However, additional examination reveals that the average current generated by each cell is in the range of 1 - 10 μA. The low current reflects the cell's high impedance, as indicated by impedance values close to 10^5 Ω on the Nyquist and Bode plots. Depending on the amount of the impedance, the current passage between two electrodes may be impeded.

  This is also connected to the electrolyte's performance. Since $FeCl_2$ precipitates quickly, the conductivity of the cell may fall dramatically throughout the measurement cycle.
- We only utilized FeCl2 and FeCl3 solutions with a concentration of 2 Mol in this experiment. This, of course, has an impact on the quantity of current generated. The utilization of a larger concentration variation in the future studies will aid in comparing the influence of electrolyte concentration on cell conductivity.
- The image has much noise most likely created by the fiber laser (shot noise). The use of a relatively small ROI region and the Fourier low pass filter are deemed ineffective in decreasing picture noise. Based on the results, there are two possibilities: first, the microscope setup used is not sensitive enough to record extremely minor signal changes; second, employing the background correction approach and background subtraction later to further eliminate noise in the image.

Chapter 7

Conclusion

To address the research question, based on the data acquired, the method use is less effective in terms of reproducibility and requires additional improvement to be employed as the basis for an optical monitoring system, since the findings obtained do not correspond to the reference. For further research, to establish a robust method, several aspects must be improved, such as:

- Utilizing a commercial sample cell
- Increase the ion concentration of the electrolyte solution
- Using alternatives background correction/background reduction methods

Bibliography

[1] H. Park, G. Kwon, H. Lee, K. Lee, S. Y. Park, J. E. Kwon, K. Kang, and S. J. Kim, "In operando visualization of redox flow battery in membrane-free microfluidic platform," *Proceedings of the National Academy of Sciences of the United States of America*, vol. 119, no. 9, pp. 1–9, 2022, ISSN: 10916490. DOI: 10.1073/pnas.2114947119.

[2] C. Zhang, L. Zhang, Y. Ding, S. Peng, X. Guo, Y. Zhao, G. He, and G. Yu, "Progress and prospects of next-generation redox flow batteries," *Energy Storage Materials*, vol. 15, pp. 324–350, 2018, ISSN: 2405-8297. DOI: https://doi.org/10.1016/j.ensm.2018.06.008. [Online]. Available: https://www.sciencedirect.com/science/article/pii/S2405829718303179.

[3] D. Aaron, Z. Tang, A. B. Papandrew, and T. A. Zawodzinski, "Polarization curve analysis of all-vanadium redox flow batteries," *Journal of Applied Electrochemistry*, vol. 41, no. 10, pp. 1175–1182, 2011, ISSN: 0021891X. DOI: 10.1007/s10800-011-0335-7.

[4] W. Wang, Q. Luo, B. Li, X. Wei, L. Li, and Z. Yang, "Recent progress in redox flow battery research and development," *Advanced Functional Materials*, vol. 23, no. 8, pp. 970–986, 2013, ISSN: 1616301X. DOI: 10.1002/adfm.201200694.

[5] M. F. Mathias, J. Roth, J. Fleming, and W. Lehnert, "Diffusion media materials and characterisation," *Handbook of Fuel Cells*, 2010. DOI: 10.1002/9780470974001.f303046.

[6] A. J. Merryweather, C. Schnedermann, Q. Jacquet, C. P. Grey, and A. Rao, "Operando optical tracking of single-particle ion dynamics in batteries," *Nature*, vol. 594, no. 7864, pp. 522–528, 2021, ISSN: 14764687. DOI: 10.1038/s41586-021-03584-2. [Online]. Available: http://dx.doi.org/10.1038/s41586-021-03584-2.

[7] E. Sánchez-Díez, E. Ventosa, M. Guarnieri, A. Trovò, C. Flox, R. Marcilla, F. Soavi, P. Mazur, E. Aranzabe, and R. Ferret, "Redox flow batteries: Status and perspective towards sustainable stationary energy storage," *Journal of Power Sources*, vol. 481, 2021, ISSN: 03787753. DOI: 10.1016/j.jpowsour.2020.228804.

[8] M. Cazot, G. Maranzana, J. Dillet, F. Beille, T. Godet-Bar, and S. Didierjean, "Symmetric-cell characterization of the redox flow battery system: Application to the detection of degradations," *Electrochimica Acta*, vol. 321, 2019, ISSN: 00134686. DOI: 10.1016/j.electacta.2019.134705.

[9] C. Doetsch and A. Pohlig, *The use of flow batteries in storing electricity for national grids*. Elsevier Ltd, 2020, pp. 263–277, ISBN: 9780081028865. DOI: 10.1016/B978-0-08-102886-5.00013-X. [Online]. Available: http://dx.doi.org/10.1016/B978-0-08-102886-5.00013-X.

[10] A. Forner-cuenca, F. R. Brushett, E. Penn, and A. M. Oliveira, "Exploring the role of electrode microstructure on the performance of non-aqueous redox flow batteries Exploring the Role of Electrode Microstructure on the Performance of Non-Aqueous Redox Flow Batteries," no. 2019, 2022. DOI: 10.1149/2.0611910jes.

[11] X. Wu, J. Hu, J. Liu, Q. Zhou, W. Zhou, and H. Li, "Conference paper Ion exchange membranes for vanadium redox flow batteries," vol. 86, no. 5, pp. 633–649, 2014. DOI: 10.1515/pac-2014-0101.

[12] A. A. Wong, S. M. Rubinstein, and M. J. Aziz, "Direct visualization of electrochemical reactions and heterogeneous transport within porous electrodes in operando by fluorescence microscopy," *Cell Reports Physical Science*, vol. 2, no. 4, p. 100 388, 2021, ISSN: 26663864. DOI: 10.1016/j.xcrp.2021.100388. [Online]. Available: https://doi.org/10.1016/j.xcrp.2021.100388.

[13] G. Tomazic and M. Skyllas-Kazacos, *Redox Flow Batteries*. Elsevier B.V., 2015, pp. 309–336, ISBN: 9780444626103. DOI: 10.1016/B978-0-444-62616-5.00017-6. [Online]. Available: http://dx.doi.org/10.1016/B978-0-444-62616-5.00017-6.

[14] N. Zimmerman, J. Campillo, and B. Frank, "VANADIUM REDOX FLOW BATTERY Sizing of VRB in electrified heavy construction equipment Master of Science Program in Sustainable Energy Systems," 2014.

[15] A. Z. Weber, M. M. Mench, J. P. Meyers, P. N. Ross, J. T. Gostick, and Q. Liu, "Redox flow batteries: A review," *Journal of Applied Electrochemistry*, vol. 41, no. 10, pp. 1137–1164, 2011, ISSN: 0021891X. DOI: 10.1007/s10800-011-0348-2.

[16] D. Koirala, N. Yensen, and P. B. Allen, "Open source all-iron battery 2.0," *HardwareX*, vol. 9, e00171, 2021, ISSN: 24680672. DOI: 10.1016/j.ohx.2020.e00171. [Online]. Available: https://doi.org/10.1016/j.ohx.2020.e00171.

[17] N. Yensen and P. B. Allen, "Open source all-iron battery for renewable energy storage," *HardwareX*, vol. 6, e00072, 2019, ISSN: 24680672. DOI: 10.1016/j.ohx.2019.e00072. [Online]. Available: https://doi.org/10.1016/j.ohx.2019.e00072.

[18] J. Huang, Y. Gao, J. Luo, S. Wang, C. Li, S. Chen, and J. Zhang, "Editors' Choice—Review—Impedance Response of Porous Electrodes: Theoretical Framework, Physical Models and Applications," *Journal of The Electrochemical Society*, vol. 167, no. 16, p. 166 503, 2020, ISSN: 0013-4651. DOI: 10.1149/1945-7111/abc655.

[19] T. Tichter, D. Andrae, J. Mayer, J. Schneider, M. Gebhard, and C. Roth, "Theory of cyclic voltammetry in random arrays of cylindrical microelectrodes applied to carbon felt electrodes for vanadium redox flow batteries," *Physical Chemistry Chemical Physics*, vol. 21, no. 18, pp. 9061–9068, 2019, ISSN: 14639076. DOI: 10.1039/c9cp00548j.

[20] P. C. Ghimire, A. Bhattarai, T. M. Lim, N. Wai, M. Skyllas-kazacos, and Q. Yan, "In-situ tools used in vanadium redox flow battery research—review," *Batteries*, vol. 7, no. 3, pp. 1–36, 2021, ISSN: 23130105. DOI: 10.3390/batteries7030053.

[21] *Bode and Nyquist Plot*, https://www.palmsens.com/knowledgebase-article/bode-and-nyquist-plot/, Accessed: 2022-12-12.

[22] D. Qu, W. Ji, and H. Qu, "Probing process kinetics in batteries with electrochemical impedance spectroscopy," *Communications Materials*, vol. 3, no. 1, pp. 1–9, 2022, ISSN: 26624443. DOI: 10.1038/s43246-022-00284-w.

[23] N. M. Bîrlea, "A power saving protocol for impedance spectroscopy," in *AIP Conference Proceedings*, vol. 1917, American Institute of Physics Inc., Dec. 2017, ISBN: 9780735416093. DOI: 10.1063/1.5018276.

[24] Y. Wu and N. Liu, "Visualizing Battery Reactions and Processes by Using In Situ and In Operando Microscopies," *Chem*, vol. 4, no. 3, pp. 438–465, 2018, ISSN: 24519294. DOI: 10.1016/j.chempr.2017.12.022. [Online]. Available: https://doi.org/10.1016/j.chempr.2017.12.022.

[25] R. Gholami Mahmoodabadi, R. W. Taylor, M. Kaller, S. Spindler, M. Mazaheri, K. Kasaian, and V. Sandoghdar, "Point spread function in interferometric scattering microscopy (iSCAT) Part I: aberrations in defocusing and axial localization," *Optics Express*, vol. 28, no. 18, p. 25 969, 2020, ISSN: 10944087. DOI: 10.1364/oe.401374. arXiv: 2006.15332.

[26] G. Young and P. Kukura, "Interferometric Scattering Microscopy," *Annual Review of Physical Chemistry*, vol. 70, pp. 301–322, 2019, ISSN: 0066426X. DOI: 10.1146/annurev-physchem-050317-021247.

[27] D. Cole, G. Young, A. Weigel, A. Sebesta, and P. Kukura, "Label-Free Single-Molecule Imaging with Numerical-Aperture-Shaped Interferometric Scattering Microscopy," *ACS Photonics*, vol. 4, no. 2, pp. 211–216, Feb. 2017, ISSN: 23304022. DOI: 10.1021/acsphotonics.6b00912. arXiv: 1611.05081.

[28] Y. Zhang and W. Huang, "Chapter 8 - soluble and low- polyimide materials," in *Advanced Polyimide Materials*, S.-Y. Yang, Ed., Elsevier, 2018, pp. 385–463, ISBN: 978-0-12-812640-0. DOI: https://doi.org/10.1016/B978-0-12-812640-0.00008-1. [Online]. Available: https://www.sciencedirect.com/science/article/pii/B9780128126400000081.

[29] Y.-H. Lin, W.-L. Chang, and C.-L. Hsieh, "Shot-noise limited localization of single 20 nm gold particles with nanometer spatial precision within microseconds," *Optics Express*, 2014, ISSN: 10944087. DOI: 10.1364/oe.22.009159.

[30] M. Khalid, I. Journal, M. K. Jasim, R. Najm, E. H. Kanan, and H. E. Alfaar, "International Journal of Science and Applied Information Technology Available Online at http://www.warse.org/ijsait/static/pdf/file/ijsait01862019.pdf Image Noise Removal Techniques : A Comparative Analysis," vol. 8, no. 6, pp. 4–9, 2019.

[31] C. Y. Cheng and C. L. Hsieh, "Background Estimation and Correction for High-Precision Localization Microscopy," *ACS Photonics*, vol. 4, no. 7, pp. 1730–1739, 2017, ISSN: 23304022. DOI: 10.1021/acsphotonics.7b00238.

[32] *Fast Fourier Transformation FFT - Basics*, https://www.nti-audio.com/en/support/know-how/fast-fourier-transform-fft, Accessed: 2022-12-25.

[33] G. Ma, Z. Wan, Y. Yang, P. Zhang, and N. Tao, "Optical imaging of single-protein size, charge, mobility, and binding," *Nature Communications*, no. 2020, ISSN: 2041-1723. DOI: 10.1038/s41467-020-18547-w. [Online]. Available: http://dx.doi.org/10.1038/s41467-020-18547-w.

[34] *WaveForms-SDK-Getting-Started-PY*, https://github.com/Digilent/WaveForms-SDK-Getting-Started-PY, Accessed: 2022-08-31.

Appendix A

List of materials

Instrument	**Specification**
Digital Multimeter and Oscilloscope	Analog Discovery 2: 100MS/s USB Oscilloscope, Logic Analyzer and Variable Power Supply
Impedance meter	Keysight E4980AL LCR Meter: 20 Hz - 1MHz
Lock-in amplifier	Unknown specification
Fiber laser	Unknown specification, $\sim 405nm$
Compact Laser Diode Drivers	Thorlabs CLD1010
Camera	Basler acA2440-35um
Lenses	Thorlabs
Beam splitter	Thorlabs
ITO glass	ITO Coated Cover, SPI 06498-AB, Slips 22x40mm, 70-100 Ω, Thickness 1.5 pk/100
ITO flexible	Unknown specification
Window layer	Double-sided sticky tape
Copper wire	Unknown specification

Table A.1: List of materials for electronic, microscope, and cell preparation setup

Appendix B

Python program

In this experiment, the Python programs are controlled the whole measurement process and analysis. All the codes is available on: https://github.com/nelfy22/thesis/tree/main/Code (will require a request for access).

B.1 Main Program

basler-video-final.py

Before running the program, a template file folder called 'f' must be transferred to local storage. Some parameters must first be configured, such as folder name, number of cycles, number of frames, frequency, offset voltage, camera exposure and image pixel size. Also, ensure that the WF SDK folder and waveform.py, which contains the Python package from Analog Discovery 2, is installed.
The program runs the measurement in 4 ON-OFF cycles simultaneously. While the cell in operation, the program will save all images in HDF5 datatype, as well as the output from the oscilloscope, which recorded in .csv datatype.

B.2 Analysis Program

iSCAT_current_response.ipynb

The program will analyze the data from the oscilloscope output to generate a graph of current response to a pulse signal.

iSCAT_variance.ipynb

The program will process the HDF5 data type and process the variance of images per dataset. It will generates a graph that correspond to the variance against the time and preview the location of expected ROI.

iSCAT_intesity.ipynb

The program process the ROI image, do filtering to images and calculate the integrated intensity of each ROI images. Then, it will generate two plots of intensity profile and FFT transformation.